Economic Geology, v. 114, no. 2, pp. 375–396

Large-Scale Stable Isotope Alteration Around the Hydrothermal Carbonate-Replacement Cinco de Mayo Zn-Ag Deposit, Mexico

Andreas Beinlich,[1, 2,†] Shaun L.L. Barker,[2, 3] Gregory M. Dipple,[2] Lyle D. Hansen,[4] and Peter K.M. Megaw[4]

[1]*The Institute for Geoscience Research (TIGeR), School of Earth and Planetary Sciences, Curtin University, Kent Street, 6845 Perth, Australia*

[2]*Mineral Deposit Research Unit (MDRU), Department of Earth, Ocean and Atmospheric Sciences, The University of British Columbia, 2207 Main Mall, Vancouver, British Columbia V6T 1Z4, Canada*

[3]*Centre for Ore Deposit and Earth Sciences (CODES), University of Tasmania, Private Bag 79, Hobart, Tasmania 7001, Australia*

[4]*MAG Silver Corp., Suite 770, 800 West Pender Street, Vancouver, British Columbia V6C 2V6, Canada*

Abstract

Carbonate-hosted hydrothermal deposits typically show narrow visible mineralogical and textural alteration halos, which inhibit exploration targeting. In contrast, hydrothermal modification of the country rock's stable isotope composition usually extends far beyond the limited visible alteration. Hence, stable isotope studies should be an effective tool to aid exploration for carbonate-hosted deposits. Here we present new insight into the development of a large stable isotope alteration halo based on 910 O and C isotope analyses of carbonate veins and hydrothermally altered limestone hosting the Cinco de Mayo Pb-Zn-Ag (Au, Cu) carbonate replacement deposit (CRD), in Chihuahua, Mexico. Our results demonstrate that stable isotope alteration is consistent with reactive, magmatic fluid flow into unaltered limestone and represents a powerful tool for the characterization of these hydrothermal ore systems. Synmineralization veins are texturally and isotopically distinct from those formed during pre- and postmineralization diagenesis and fluid flow and show distinct gradients along the direction of mineralizing fluid flow: this appears to be a promising exploration vectoring tool. Downhole variations in wall-rock isotope values reveal aquifers and aquicludes and outline the principal hydrothermal flow paths. Furthermore, wall-rock $\delta^{18}O_{VSMOW}$ systematically decreases toward mineralization from ~23‰ to <17‰ over a distance of ~10 km, providing another vectoring tool. The extent of the stable isotope alteration halo likely reflects the overall fluid volume and areal extent of a fossil hydrothermal system, which may be expected to scale with the mineral endowment. This suggests that constraining the size, shape, and degree of isotopic alteration has direct application to mineral exploration by outlining the system and indicating the potential size of a deposit.

Introduction

The stable isotope compositions of natural fluids and rocks are generally different, so mineral replacement reactions occurring during hydrothermal rock alteration often result in distinctly modified isotope ratios ($\delta^{18}O$, $\delta^{13}C$) of the affected rock relative to its precursor (Taylor and Epstein, 1963; Taylor, 1974, 1979; Larson and Taylor, 1986a; Klein and Criss, 1988; Cathles, 1993). Mapping the spatial distribution of stable isotope alteration has been successfully employed to constrain the size of fossil hydrothermal systems and the controls on fluid migration, their origin, volume, and compositional evolution (Larson and Taylor, 1986b; Larson et al., 1994; Campbell and Larson, 1998). Hydrothermal ore deposit formation involves large volumes of disequilibrium fluids that interact with the country rock, causing halos of isotopic alteration (e.g., $\delta^{18}O$ and $\delta^{13}C$) that show values distinct from more distal, unaltered rocks. These disequilibrium fluids also commonly deposit secondary carbonate veins with distinct isotopic values. The spatial extent of isotopic alteration and isotopically distinctive carbonate veins usually extends far beyond zones of visible alteration and metal enrichment (e.g., Criss et al., 1985). Therefore, stable isotope mapping represents a potentially powerful prospecting tool complementing other mineral exploration techniques (e.g., mineralogy, lithogeochemistry, geophysics) (see also Criss and Taylor, 1983; Larson et al., 1994). The extent and degree of isotopic alteration of a given host rock depends on the fluid transport mode (pervasive or channelized), fluid and rock composition, fluid volume, and temperature-dependent reaction kinetics (e.g., Lassey and Blattner, 1988; Frimmel, 1992). Hydrothermal limestone alteration typically develops very limited visible alteration zones immediately around fluid-flow paths, hence stable isotope studies in exploration for carbonate-hosted hydrothermal ore deposits are particularly attractive (see also Shelton, 1983; Ewers et al., 1994; Kesler et al., 1995; Taylor, 1997; Vazquez et al., 1998; Waring et al., 1998; Criss et al., 2000; Large et al., 2001; Kelley et al., 2006). Even though stable isotope studies can yield critical constraints on fluid composition and source, alteration temperature and size of the hydrothermal system, their practical application is surprisingly limited to only one successful documented discovery (Naito et al., 1995). Historically, the main reasons for the limited practical deployment of stable isotope mapping in mineral exploration were unacceptably high costs of data collection and long turn-around times. Consequently, stable isotope studies of hydrothermally altered country rocks have been limited to purely academic research despite the potential for improving mineral exploration in some environments (Criss and Taylor, 1983; Dilles et al., 1992; Jamtveit et al., 1992; Larson et al., 1994; Murakami and Nakano, 1999; Barker et al., 2013; Hickey et al., 2014; Millonig et al., 2017).

†Corresponding author: e-mail, andreas.beinlich@curtin.edu.au

ISSN 0361-0128; doi: 10.5382/econgeo.2019.4635; 22 p.

Submitted: August 16, 2018
Accepted: February 26, 2019

This study aims to further the understanding of how the stable isotope compositions of hydrothermally altered limestone can be used as a vectoring tool in carbonate replacement deposits (CRDs) through use of an off-axis integrated cavity output spectrometer (OA-ICOS) that allows for high sample throughput at minimal analytical cost (Barker et al., 2011, 2013; Beinlich et al., 2017). Vein and wall-rock carbonate samples (n = 910) from 16 drill holes around the Cinco de Mayo Upper Manto mineralization were examined and analyzed for textural characteristics and isotope and trace-element compositions to define the overall extent of the stable isotope alteration footprint, identify fluid and metal transport pathways, and to assess the transitions in stable isotope signatures from proximal intrusion-related skarn to distal carbonate-hosted manto systems. The results provide new constraints on the volume of alteration fluids, their composition and source, and the critical dimensions of fluid transport in a large hydrothermal system.

Geologic Context

General overview

The Cinco de Mayo Zn-Ag CRD is located in the State of Chihuahua, Mexico, approximately ~190 km north of the capital, Chihuahua City (Robertson and Megaw, 2009). Cinco de Mayo is one of a family of CRDs that define a belt 2,200 km long along the interface between the Tertiary volcanic plateau of the Sierra Nevada Occidental and the Laramide Mexican thrust belt (Megaw et al., 1988). The most significant CRDs are hosted in carbonate successions of the Chihuahua and Sierra Madre terranes, which together with the Coahuila and Maya terranes are underlain by Paleozoic or possibly older continental crust (Ruiz et al., 1988). Mineralization throughout the belt occurs in a limestone-dominant transgressive sedimentary succession deposited during Jurassic-Cretaceous flooding of pre-middleTriassic basement terranes (Haenggi, 2002). This basement was block-faulted during middle-Jurassic extension, creating a series of linear basins, including the NW-elongate Chihuahua trough, which controlled sedimentation (Megaw et al., 1996). The deposit is situated at the western boundary of the Chihuahua trough where E-dipping thrust sheets of Cretaceous limestone, shale, and sandstone were stacked by basin inversion during NE-SW–directed Laramide compression between ~84 and ~43 Ma (Muehlberger, 1993). This NE-SW compression was accompanied by gentle to tight folding and extensive axial faulting and fracturing (Hewitt, 1966; Handschy and Dyer, 1987) that created structurally enhanced permeability subsequently exploited by mid-Tertiary intrusions ranging in composition from diorite through rhyolite. Hydrothermal fluids related to these magmas also followed these deformation zones; depositing a range of skarn, CRD, and vein deposits (Clark and de la Fuente L., 1978; Megaw et al., 1988). Megaw et al. (1988) noted that mineralization is commonly hosted in limestone layers capped by impermeable strata that confined fluid flow and mineral precipitation to distinct zones. Lead isotope data from mineral deposits in northern Mexico suggest mixing of reworked Pb from the underlying Precambrian basement and magmatic Pb from the Cenozoic mantle linked to rapid spreading at the East Pacific Rise prior to the opening of the Gulf of California (McDowell and Keizer, 1977; Cumming et al., 1979; Megaw et al., 1996; Nieto-Samaniego et al., 1999). The timing of mineralization throughout the region is bracketed between 57.9 and 25.9 Ma, coinciding with the main period of the Tertiary Sierra Madre Occidental volcanic activity, with maxima between 35 and 29 Ma (Megaw et al., 1988; Albinson et al., 2001; Camprubi et al., 2006; Velador et al., 2010).

The Cinco de Mayo CRD

Cinco de Mayo is an Ag-Pb-Zn CRD recently discovered within a 25,000-hectare concession 100% owned by MAG Silver Corp. The property is centered on the Sierra Santa Lucia, a 4-km-wide, 15-km-long ridge composed of imbricated NW-striking, E-dipping thrust sheets of Cretaceous limestone, sandstone, and shale (Fig. 1). The thrusting and folding were developed during Laramide compression (ca. 55 Ma), roughly 25 m.y. before the interpreted age of mineralization, and little to no evidence for postmineral structural offsets has been seen anywhere in the project area (Lyons, 2009) The sierra is surrounded by a flat, featureless alluvial plain that stretches for several kilometers in all directions. This plain is interrupted on its east side by an isolated 0.5-km-wide × 2.0-km-long NW-elongated ridge of east-dipping limestone (Cinco de Mayo Ridge), which is cut by numerous mineralized jasperoid veins (Robertson and Megaw, 2009). Exploration began in 2004 along this ridge and rapidly progressed into the surrounding covered areas, guided by repeated iterations of geological interpretation, airborne geophysical surveys, and drilling.

The known mineralization is hosted within Lower Cretaceous limestone along NW-SE– and lesser NE-SW–trending structures, dominantly where juxtaposed against impermeable Upper Cretaceous shales and sandstones of the Benavides and Ojinaga Formations (Table 1; Lyons, 2009). Mineralization occurs as relatively flat lying to E-dipping sheetlike massive sulfide "manto" (Spanish for "cloak" or "blanket") replacement bodies in the limestone with sulfide mineralized veinlets in the hanging-wall shales and sandstones. In many areas these shales are metamorphosed to hard, compact pyritic hornfels. Mantos consist of massive fine- to coarse-grained pyrite, pyrrhotite, galena, and sphalerite, with minor chalcopyrite and acanthite. Domains of unreplaced limestone are common within the massive sulfides. Common gangue minerals include barite, fluorite, quartz, and abundant manganoan calcite (Megaw et al., 2014). Coarse-grained sulfide-mineralized veinlets dominated by manganoan calcite occur along vein walls, in calcite-cemented breccia, and as stringers replacing the vein calcite. Sulfide minerals are commonly banded, mimicking sedimentary features of the precursor limestone, and they frequently show intramineral brecciation, remineralization, and recrystallization, indicating multiple pulses of mineralizing fluids. With depth, mineralization becomes surrounded by recrystallized limestone that grades progressively to coarse-grained marble, with massive, pervasively hydrated garnet-pyroxene skarn appearing at depth. Aphanitic felsic dikes, typically less than 10 m thick and locally showing flow-banding or fluidal breccia textures, were encountered in three areas along the principal 10-km-long mineralized trend. In all three places these dikes are in direct contact with, or are found within, massive sulfide mineralization and/or sulfide-mineralized garnet-pyroxene skarn carrying trace scheelite

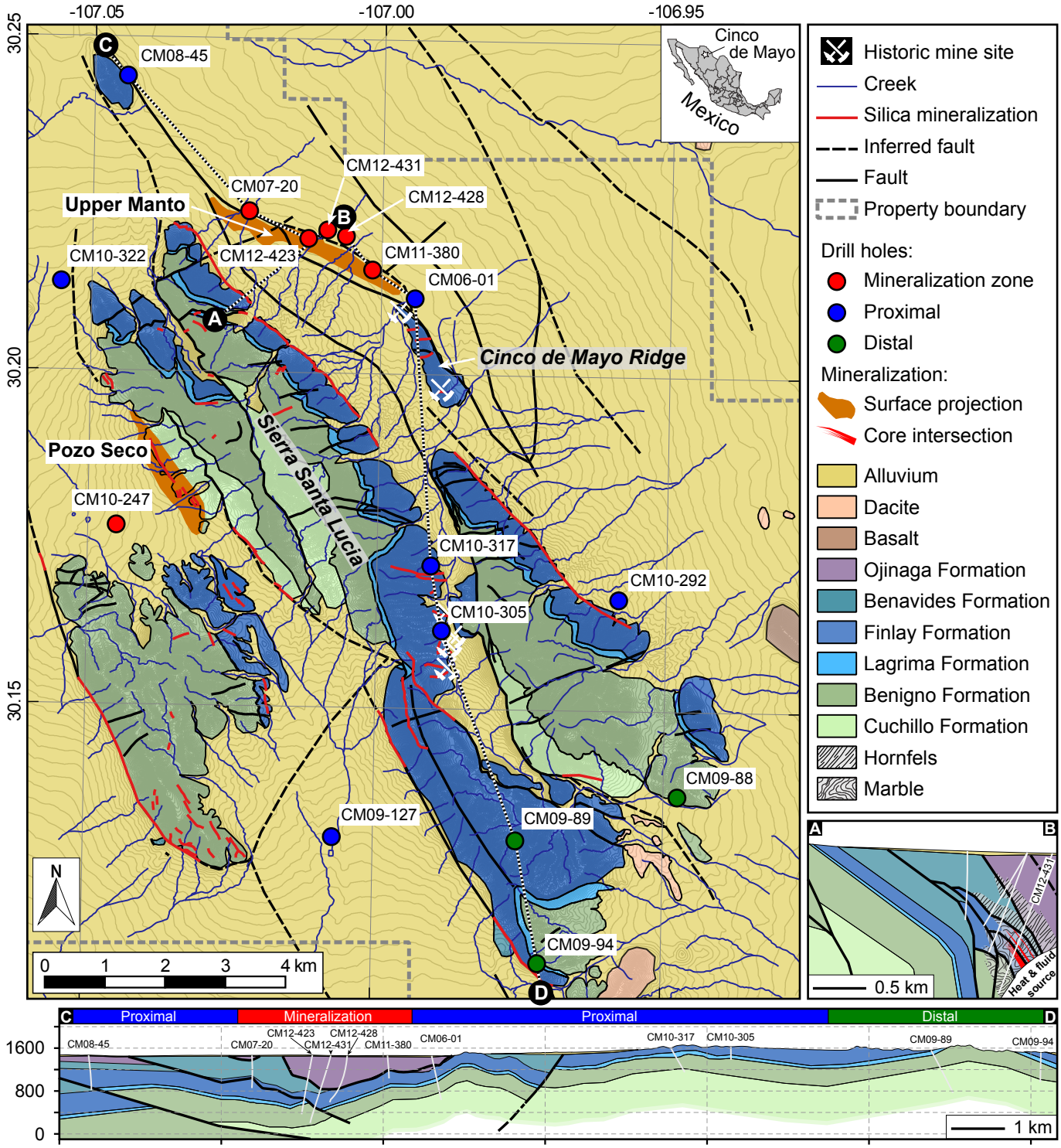

Fig. 1. Geologic map of the Cinco de Mayo property showing the location of investigated drill holes and surface projection of the Upper Manto and Pozo Seco zone mineralization. Cross and longitudinal sections show subsurface details of the mineralized zone (A-B) and the aquifer system (C-D) across and along strike, respectively, and are based on drill core data. Unlabeled drill holes in the cross section are not discussed in the text. Depth extrapolation of the local stratigraphy in the southern part of the Cinco de Mayo property is uncertain and hence omitted from the longitudinal section. Mineralization and hornfels and marble alteration near CM12-431 are shown only in the cross section (A-B) and omitted from the longitudinal section (C-D) for clarity. Note that mineralization exclusively occurs in the Finlay Formation. The deepest part of mineralization intersected by CM12-431 is termed Pegaso zone, the shallower mineralization is termed Upper Manto (labels were omitted from the cross section for clarity). Note that a large part of the property is covered by a veneer of alluvium that is difficult to see at the scale of the cross and longitudinal sections.

Table 1. Summary and Description of Limestone Formations at Cinco de Mayo

Formation	Age	Description	Thickness (m)
Ojinaga	Turonian	Immature volcanogenic sandstones and mudstones with scattered conglomerate horizons composed of clasts of volcanic and sedimentary origin; mudstones vary from red (subaerial source) to green (subaqueous source) and mostly lack internal texture	>300
Benavides	Late Albian	Medium gray, argillaceous limestone to variably fossiliferous and calcareous shale sequence; indicative alternation of dark gray calcareous shale with light gray micritic limestone on the tens of meter scale	~300–400
Finlay	Middle Albian	Medium gray carbonate with variable fossil content and black chert; carbonate ranges from micrite to sparite and calcarenites; the upper 20 m sometimes contain a storm rip-up clast horizon producing permeability and is frequently characterized by hematite stained solution cavities, coarse white calcite, and chalcedony-quartz deposits; this zone as well as the upper and lower stratigraphic contacts are the main loci for mineralization	~100–200
Lagrima	Middle Albian	Black calcareous shale to dark gray, variably fossiliferous argillaceous limestone; the black shale dominates in drill core and frequently contains thin beds of limestone	~30–100
Benigno	Early Albian	Medium gray carbonate with variable fossil content, variable black chert and minor shale partings; within the district, the Benigno Formation is capped by a very distinctive, strongly bioturbated carbonate mud transition zone from the Lagrima Formation; the carbonate ranges from micrite to sparite displaying a rich biotic carbonate mud-supported reef environment	~200–300
Cuchillo	Aptian	Alternating 1- to 20-m-thick limestone beds interbedded with calcareous black shale of equal thinkesses	>500

(Megaw et al., 2014). The only other intrusive rocks seen in the area are demonstrably premineral intermediate composition dikes and sills that occur throughout the range and were cut in drill holes at the northwest tip of the Sierra Santa Lucia. Regional high- and low-altitude, district-scale high-resolution airborne magnetic surveys show large and strong magnetic highs underlying the Sierra Santa Lucia; these are interpreted as reflecting a large-scale intrusive system at depth (Robertson and Megaw, 2009).

The mineralization defined to date occurs in imbricated east-dipping slices of limestone along the NW-trending, E-dipping Jose thrust fault. As drilling progressed it emerged that, in detail, the Jose thrust fault consists of several individual strands that overlap one another progressively to the southeast, creating repetitions of slices of the host limestones on both the hanging and footwalls of the individual strands. Locally, the limestones are in contact with each other across the faults, effectively creating continuous limestone domains around the faults, but slices of the overlying shale and sandstone units insulate the limestone slices from each other.

Initial drilling at Cinco de Mayo Ridge in 2007 intersected minor massive sulfide hosted in limestone of the Lower Cretaceous Finlay Formation and massive hornfels alteration cut by dispersed and veinlet Zn-Pb sulfide mineralization in shales of the Upper Cretaceous Benavides Formation on opposite sides of one strand of the Laramide thrust fault (Robertson and Megaw, 2009). Continued drilling between 2007 and 2012, starting 4 km to the northwest and working back southeastward toward Cinco de Mayo Ridge discovered and defined the "Upper Manto," a continuous, NW-elongate, east-dipping tabular body of massive sulfide mineralization averaging 5 m thick, 450 m downdip and 4,000 m long (Fig. 1). Three holes drilled beneath the northwestern end of the Upper Manto encountered dikes of white, aphanitic rhyolite similar to those seen in many CRDs (Megaw et al., 1988; Megaw, 1990). These are the only intrusions seen to date along the Upper Manto and they occur within or directly in contact with massive sulfide and scheelite-bearing hydrated garnet-pyroxene skarn. One of these dikes has a matrix-supported breccia offshoot composed of aligned, highly angular, tabular dike fragments that locally flow around larger dike and wall-rock breccia fragments. Similar skarn and sulfide-related aphanitic rhyolite dikes were cut in the La Gloria area along the projection of the Jose thrust about 2 km southeast of Cerro Cinco de Mayo and in the Polaris area 3 km distant at the extreme northwest end of the Sierra Santa Lucia.

Although mineralization in the Upper Manto is continuous over its 4-km length, mineralization affects the limestone of two adjacent premineral thrust sheets; the northwest half of the manto lies in the western sheet and the southeastern half lies in the eastern sheet. Continuous mineralization affects limestone in both slices where the two sheets overlap and mineralization shifts from the eastern to the western thrust sheet. Mineralization in both segments deepens toward this overlap zone, creating a "gull-wing" pattern (Fig. 1). This pattern suggested that mineralizing fluids rose along this overlap zone and spread laterally into the individual sheets, so in mid-2012, drill hole CM12-431 was directed deep (1,200 m) into this overlap zone. At about 850-m depth, three major massive sulfide zones (3.12, 20.15, and 61.6 m in core length) were cut within an overall 93-m span (Fig. 1). The thickest and deepest intercept (the Pegaso zone; 61.1 m) graded 89 g/t silver, 0.78 g/t gold, 0.13% copper, 2.1% lead, and 7.3% zinc (MacInnis, 2012). The mineralization occurs within a 400-m-thick zone of pervasive skarn and marble, but despite the pervasive skarn and marble development, no intrusions were cut in the hole. The mineral resources estimated for the Upper Manto based on available drill hole data as of September 1, 2012, amount to 12.45 million tonnes of 132 g/t Ag, 0.24 g/t Au, 2.86% Pb, and 6.47% Zn. The estimated total resource consists of 52.7 Moz of silver, 785 Mlb of lead, 1,777 Mlb of zinc, and 96,000 oz of gold (Ross, 2012).

Despite the fact that the major mineralization zone is completely blind, with no outcrop expression whatsoever, the drilling density (>250 holes) is sufficient to confidently show continuous mineralization from the Upper Manto to the Pegaso zone (MacInnis, 2010, 2012). This continuous mineralization shows a classic metal zonation pattern from silver, lead, and zinc with low gold and very low copper near the surface to increased zinc, gold, copper, and tungsten, with a concomitant decrease in lead and silver at depth. This follows the megascopic alteration patterns of (1) downwardly increasing recrystallization and marbelization of the limestone, (2) the appearance of skarn at depth, and (3) increased development of hornfels in the hanging-wall shales toward the Pegaso zone. Subtler features, such as a downward increase in the size of pyrrhotite crystals (mm to cm) and the size of pyrite crystals replacing the pyrrhotite are also present, reinforcing the interpretation of continuous zoning from near surface to depth into the Pegaso zone. Furthermore, the metal and alteration zonation at Cinco de Mayo is consistent with that encountered in classic Zn skarn and other Mexican CRDs including Fe and Mn enrichment in proximal, mineralization-related calcite veins (Megaw et al., 1988; Meinert et al., 2005).

Concurrent exploration through virtually complete alluvial cover on the west side of the Sierra Santa Lucia about 4 km to the SW of the Upper Manto, discovered the Pozo Seco mineralization in 2008 (Fig. 1). Pozo Seco lies directly along another major NW-striking thrust, but the Pozo Seco fault dips vertically to steeply west, probably reflecting overturning (Lyons, 2009). Initially revealed by an airborne versatile time domain electromagnetic (VTEM) geophysical survey as a sharp, 10-km-long linear anomaly, this structure was ultimately traced by drilling for over 5 km with the 2.5-km-long Pozo Seco molybdenum-gold body lying within it. Pozo Seco consists of a tabular, strongly ferruginous Liesegang-banded jasperoid body, ~2.5-km long, 250 to 300-m wide, and 17 to 250-m thick, carrying average grades of 0.15% Mo and 0.25 ppm Au (MacInnis, 2009, 2010). The molybdenum in this unusual body occurs principally as powellite on fracture surfaces, while the gold occurs native within very fine grained quartz veinlets. The gold and molybdenum mineralization are not consistently coincident, indicating they are products of separate pulses of mineralizing fluids.

Local stratigraphy

Mineralization at Cinco de Mayo is related to an interplay between ore fluids related to Cenozoic silicic magmatism (reflected by the aphanitic rhyolite dikes) moving along structures generated during Laramide deformation that cut a thick sequence of Jurassic-Cretaceous limestones, clastic sediments, and evaporates deposited in the Jurassic Chihuahua trough. The principal mineralization hosts are fossiliferous limestone units of the well-studied Albian-Aptian-Cenomanian (Cretaceous) Chihuahua trough sequence (Table 1) ranging from the late Aptian Cuchillo Formation, overlain in turn by the Benigno, Lagrima, and Finlay Formations. The Finlay Formation is the most important host for mineralization; it is a relatively clean limestone with local cherty beds, high energy beach zones, and reefs (Lyons, 2009). The Finlay Formation is also the principal host unit for mineralization in other CRDs in Chihuahua, including Santa Eulalia and Naica, where its stratigraphic relationships, lithologic characteristics, and isotopic characteristics have been studied in detail (Hewitt, 1966; Sweeney, 1987; Megaw, 1990). The overall limestone sequence grades downward into evaporites dominated by gypsum and/or anhydrite with interbedded shale, whereas a more abrupt change to shale and clastic sediments composed of conglomerate, sandstone, and siltstone of the overlying Benavides and Ojinaga Formations caps the sequence. These impermeable and unreactive units, especially the latest Albian Benavides Shale, may have played an important role as an aquitard capping hydrothermal fluid movements during mineralization (Selway and Leonard, 2008). The uppermost Albian and Cenomanian Del Rio and Loma de Plata Formations of the regional stratigraphy are not reported in outcrop at Cinco de Mayo, but have been cut in drilling (Lyons, 2009).

Methods

Macroscopic investigation

For initial investigation, half-core samples were chosen based on downhole location to allow for even spacing, with increased density near mineralization. Subsequent sampling focused on vein–wall-rock pairs from the Finlay Formation. Samples were photographed under normal and UV light to identify microsampling sites and distinct vein generations based on UV fluorescence color and intensity, crosscutting relationships, deformation features, and the macroscopic appearance of the vein–wall-rock interface.

Samples

Wall-rock carbonate and vein calcite samples were taken from half-core from 16 drill holes located through the NW-SE–trending Upper Manto and along a ~12 km NNW-SSE–trending transect from the Upper Manto to the most distal drill hole in the far SE corner of the Cinco de Mayo property (Fig. 1). Six additional drill holes from the vicinity of the two transects were also sampled. Based on the location relative to the mineralization, these drill holes are labeled "mineralization zone," "proximal," and "distal," respectively. Mineralization zone samples are dominantly from the Upper Manto (CM07-20, CM12-423, CM12-431, CM12-428, and CM11-380) together with additional samples from Pozo Seco (CM10-247). Proximal samples are dominantly from drill holes located to the south and southeast of the Upper Manto (CM06-01, CM10-317, CM10-305, CM10-127, and CM10-292) and define a transect bridging the area between the mineralization and the distal drill holes (CM09-88, CM09-89, and CM09-94) in the southeast corner of the property. This transect is parallel to the general strike of thrusting in the area and was chosen to discern the extent of fluid flow and stable isotope alteration in the subsurface. CM08-45 is located to the northwest of the Upper Manto and was regarded as the "most barren looking hole" on the Cinco de Mayo property during exploration drilling (Megaw, pers. commun.) and was initially expected to reflect the local stable isotope background. However, its stable isotope values fall in the "proximal" range. Thus, CM09-94, which shows the least isotopically altered values, was taken as the stable isotope background against which the compositions of all other samples are compared.

Stable isotope analyses were conducted on carbonate powder drilled from selected sites on solid half-core samples using a handheld Dremel™ tool. The drill bit was cleaned in 10% HCl and ethanol after each sample to avoid cross-contamination between samples. Sites for microsampling were chosen based on macroscopic investigation of half-core samples under normal and UV light and assay data provided by MAG Silver. Microsampling sites include different vein generations and their respective wall rocks.

Initial sampling aimed at defining the overall variability of stable isotope data with depth and also with distance from the known location of mineralization. This was achieved by systematic sampling over large depth intervals (e.g., CM11-380: 150 m; CM09-89: 867 m) and across formation boundaries every ~7 m. The depth spacing between sampling sites was reduced to ~2 m near mineralization. At larger vertical distance from mineralization, the sample spacing was occasionally increased to ~10 m. This sampling approach was applied to CM12-423, CM12-431, CM10-247, CM11-380, CM10-305, CM09-88, CM09-89, and CM09-94. Figure 2 shows examples of the sample spacing with depth in CM12-431 and CM09-94. Subsequent sampling focused mostly on the Finlay Formation. Where possible, both wall-rock limestone and vein calcite were sampled as pairs from the same half-core sample. For these sample pairs, the distance between wall rock and vein drill spots was typically between 1 and 3 cm. Sampled formations include Cuchillo, Benigno, Lagrima, Finlay, and Benavides. Tables 2 and 3 provide an overview of the number of vein and wall-rock samples per core and formation.

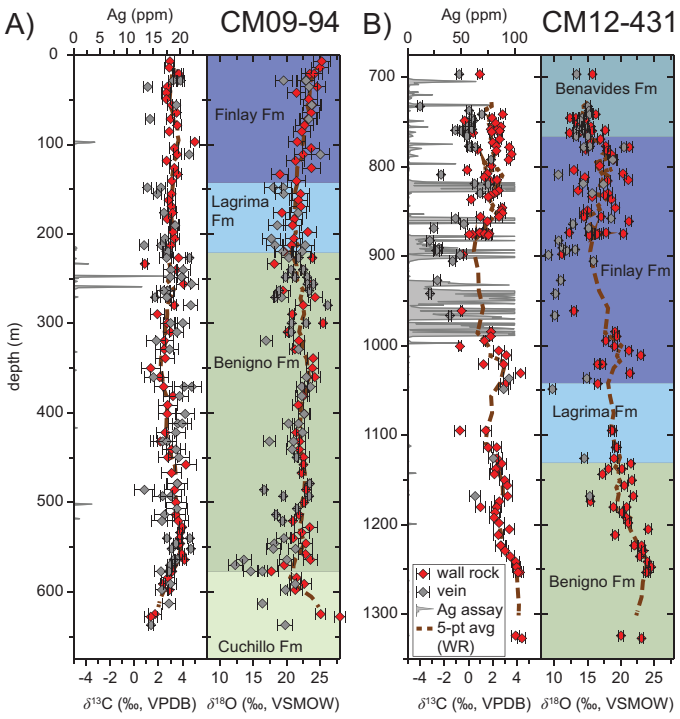

Fig. 2. Downhole O and C isotope ratios in wall-rock and vein calcite samples from (A) the least altered hole (CM09-94) and (B) the mineralization zone (CM12-431). The brown dashed line represents the five-point moving average for wall-rock $\delta^{18}O$ and $\delta^{13}C$ values. The bulk rock Ag concentration (ppm; secondary abscissa) is displayed as a proxy for mineralization.

Stable isotope analysis

Approximately 35 mg of carbonate powder was placed into unflushed 12-mL Labco borosilicate glass vials that were sealed with butyl rubber septa. About 15 drops of 85% H_3PO_4 were injected into each vial through the rubber septum and left to react with the carbonate powder for ~1 hour on an aluminium block heated to 72°C. Following digestion, sample gas released from the dissolved carbonate was introduced into an OA-ICOS; Los Gatos Research (LGR) model 908-0021 and CCIA-46 via a stainless steel tubing line with a cold trap (~–78°C) to freeze out water vapor (Barker et al., 2011). The OA-ICOS instrument simultaneously measures the volume fraction of CO_2 isotopologues ($^{12}C^{16}O^{16}O$, $^{13}C^{16}O^{16}O$, $^{12}C^{16}O^{18}O$) by high-resolution laser absorption in the near-infrared range. A more detailed summary of the OA-ICOS theory and its application to carbonate minerals can be found in Baer et al. (2002) and Barker et al. (2011). LGR model 908-0021 is incapable of accurately measuring the isotope composition of CO_2-H_2S mixtures, which results from acid digestion of sulfide-bearing carbonate samples. These samples were analyzed using a second generation ICOS instrument (LGR CCIA-46), equipped with a modified laser system that avoids laser absorption by H_2S (Beinlich et al., 2017). The stable isotope composition is reported as δ-values in per mil (‰), i.e., as parts per thousand difference from a standard (Faure and Mensing, 2005):

$$\delta X = [(R_{sample}/R_{standard})-1] \times 10^3,$$

where X denotes ^{13}C or ^{18}O and R is $^{13}C/^{12}C$ and $^{18}O/^{16}O$, respectively. Throughout the text we describe relatively high δ-values as "enriched" and relatively low δ-values as "depleted." Repeated analyses of the UBC-MDRU calcite in-house standard BN13 indicate that the measurements are accurate with a standard error of 0.6‰ (1 SE) for $\delta^{18}O$ and 0.5‰ (1 SE) for $\delta^{13}C$ (Barker et al., 2011). All isotope values in this report are standardized to Vienna Standard Mean Ocean Water (VSMOW) and Vienna Pee Dee Belemnite (VPDB) for oxygen and carbon, respectively. Every analytical session began and was ended with four analyses of the BN13 standards, which was also run intermittently after every sixth unknown sample. Additional standards were run as unknowns for quality control. The memory effect was mitigated by pump-flush cycles (two cycles for the ICOS cell, six cycles for the vacuum line) between analyses using CO_2-free "zero gas" produced by scrubbing water vapor and CO_2 from ambient air through a series of Drierite™, soda lime, Sofnolime,™ and Ascarite™ filled columns (Beinlich et al., 2017). The standard deviation given in the text refers to the 68% confidence interval (1σ). A total of 910 O and C isotope analyses were conducted for this study.

Trace-element analysis

Laser ablation ICP-MS measurements of a series of trace elements was carried out using a ASI Resolution S155-SE laser ablation system, based on a 193-nm ArF excimer laser (ATL) attached to a N_2 purged-beam delivery unit at the University of Waikato, New Zealand. A spot size of 100 µm and laser fluence of ~6 J cm^{-2} was used. Ablation took place in a two-volume cell, developed by Laurin Technic (Müller et al., 2009). Before analysis, the cell was vacuum purged

Table 2. Average Carbon and Oxygen Isotope Composition of Limestone Wall Rock (WR) and Vein Samples Outside the Finlay Formation

	Benavides					Lagrima					Benigno					Cuchillo				
	δ^{13}C (‰, VPDB)	s.d. δ^{13}C	δ^{18}O (‰, VSMOW)	s.d. δ^{18}O	n	δ^{13}C (‰, VPDB)	s.d. δ^{13}C	δ^{18}O (‰, VSMOW)	s.d. δ^{18}O	n	δ^{13}C (‰, VPDB)	s.d. δ^{13}C	δ^{18}O (‰, VSMOW)	s.d. δ^{18}O	n	δ^{13}C (‰, VPDB)	s.d. δ^{13}C	δ^{18}O (‰, VSMOW)	s.d. δ^{18}O	n
CM09-94 WR						3.1	0.2	21.2	1.2	10	3.1	0.8	22.2	1.6	38	2.2	0.7	23.7	2.8	5
CM09-94 veins						2.2	0.8	19.8	1.9	10	3.3	0.9	20.4	2.8	48	2.4	0.7	19.3	2.1	4
CM09-88 WR											2.8	1.7	22.0	1.3	19	2.7	1.1	18.2	2.3	12
CM09-88 veins											0.2	4.3	19.4	2.8	12	1.3	0.8	16.7	2.4	9
CM09-89 WR						2.5	0.4	20.5	1.2	9	3.7	0.5	21.0	1.5	36	3.4	0.6	20.8	1.6	32
CM09-89 veins						1.7	0.4	18.7	1.0	3	3.2	1.5	20.6	1.5	22	3.3	0.8	20.5	1.4	23
CM09-127 WR	2.1	0.7	19.0	1.6	5	2.7	0.5	15.5	1.6	3	2.4	0.3	20.3	0.4	4					
CM09-127 veins	1.3	1.8	17.2	2.1	4	1.8	0.6	16.8	2.1	3										
CM10-292 WR						1.6	2.3	21.7	6.2	2	2.5	0.6	22.5	3.2	3					
CM10-292 veins						2.1	1.0	15.5	11.9	2	1.4	0.9	20.3	0.6	2					
CM10-305 WR						3.9		17.8		1										
CM10-305 veins						3.6		9.7		1										
CM11-380 WR						3.1	0.4	17.9	2.9	7										
CM11-380 veins						1.5	1.5	17.1	3.2	8										
CM12-423 WR						2.0	1.2	18.5	1.8	16	2.3	0.5	21.8	1.6	18					
CM12-423 veins						0.7	0.6	16.0	2.1	12	1.9	0.8	21.3	5.1	3					
CM12-431 WR	1.8	1.0	14.7	1.6	12						2.7	1.1	20.9	2.3	30					
CM12-431 veins	–0.4	1.2	14.3	0.7	14						1.8	1.2	13.2	3.0	3					
CM10-247 WR						1.8	1.1	14.4	1.0	7	2.6	1.1	16.0	2.0	35	3.0	0.5	14.4	1.0	7
CM10-247 veins						0.2	2.0	17.3	1.0	5	1.6	1.2	15.2	5.3	27	2.0	0.8	15.9	2.4	13

The standard deviation (1σ) reflects the spread of the overall data population

Table 3. Average Carbon and Oxygen Isotope Composition of Finlay Limestone Wall-Rock and G2 Vein Samples

	Wall rock					G2 veins					
Core ID	$\delta^{13}C$ (‰, VPDB)	s.d. $\delta^{13}C$	$\delta^{18}O$ (‰, VSMOW)	s.d. $\delta^{18}O$	*n*	$\delta^{13}C$ (‰, VPDB)	s.d. $\delta^{13}C$	$\delta^{18}O$ (‰, VSMOW)	s.d. $\delta^{18}O$	*n*	Distance from CM12-431 (km)
Distal cores											
CM09–94	3.3	0.6	23.0	1.5	19	3.1	1.1	22.5	1.7	5	12.7
CM09–88	Finlay Formation not present in CM09-88										11.1
CM09–89	2.9	0.8	22.9	2.3	11	2.8	1.3	21.0	0.7	7	10.6
Proximal cores											
CM09–127	3.7	0.2	19.5	0.6	4	2.9	0.5	18.6	0.3	2	10.1
CM10–292	2.2	1.1	18.7	2.0	10	1.9	1.1	14.8	2.5	5	7.8
CM10–305	1.4	2.2	18.9	2.1	29	0.7	2.5	18.0	0.7	5	6.9
CM10–317	1.2	2.1	20.8	1.3	13	No G2 veins present in CM10-317					5.9
CM10–332	1.0	1.2	15.5	2.9	9	2.5	0.6	11.9	1.5	9	4.5
CM08–45	1.1	1.3	16.6	2.1	15	1.1	1.6	16.4	2.4	9	4.1
CM06-01	1.7	2.0	17.9	2.5	13	–0.2	2.7	16.9	1.5	6	1.8
Mineralization zone cores											
Upper Manto											
CM07-20	2.1	1.6	15.6	2.5	3	1.0	1.9	15.9	2.0	3	1.4
CM11-380	2.6	1.0	17.4	3.2	27	–0.8	1.4	12.9	2.7	13	1.0
CM12-423	1.9	1.2	19.6	2.2	49	0.4	0.8	15.9	1.3	13	0.3
CM12-428	1.9	0.9	17.2	3.8	6	0.3	1.3	16.5	1.7	5	0.3
CM12-431	1.8	1.2	17.2	2.7	43	–0.8	1.9	13.9	3.2	21	0.0
Pozo Seco orebody											
CM10-247	2.5	0.7	14.5	1.3	25	–0.5	1.1	13.2	1.5	8	6.0

The standard deviation (1σ) reflects the spread of the overall data population

and then filled with He, which washed the ablated aerosol out of the cell. The carrier gas was mixed with Ar in the cone that sits above the zone where ablation takes place, and was then mixed downstream with a small amount of N_2 (6 mL/min) to increase plasma temperature (Hu et al., 2008). The ablation aerosol was transported through a nylon manifold signal-smoothing device ("squid") before reaching the torch of a Perking Elmer Elan II ICP-MS. The ICP-MS was tuned using NIST 612 glass for high sensitivity and low oxide production rates (ThO/Th <0.5%). The quadrupole mass analyzer sequentially peak shifts between masses of interest (Mg, Si, P, S, Mn, Fe, Cu, Zn, As, Sr, Y, Ba, La, Ce, Pr, Nd, Sm, Eu, Gd, Tb, Dy, Ho, Er, Tm, Yb, Hf, Tl, Pb, Th, U) during the laser ablation process, with a sweep time over the entire mass range of less than 1 second. 40 seconds of laser ablation data were collected for each analysis point, and at least 20 seconds of gas blank were collected for each sample. The ICP-MS collected data continuously in time-resolved analysis mode, with gas blanks collected before and after each laser ablation point to facilitate blank subtraction. NIST 612 was used as a calibration standard. Data reduction followed established protocols for time-resolved analysis (Longerich et al., 1996). Iolite software (Hellstrom et al., 2008) was used for data reduction, with ^{43}Ca used as an internal standard. Carbonate minerals were assumed to be pure calcite, with Ca = 40.04 wt % for the internal standard. As laser ablation ICP-MS results are reported relative to the external standard value, a ±5% variation in this value will lead to an uncertainty of ~13% in the calculated trace-element concentrations.

Results

Stable isotope analysis was initially focused on identifying the preferential fluid flow path at Cinco de Mayo. Based on the variability and absolute values of stable isotope ratios, we identified the Finlay Formation as the principal aquifer affected by the hydrothermal fluids, which then became the main focus of subsequent sampling. The downhole distribution of O and C isotope ratios in vein and wall-rock samples of the most mineralized drill hole (CM12-431) was compared with that of the least-altered drill hole (CM09-94) in Figure 2, showing the distribution of stable isotope ratios across several limestone formations. The stable isotope ratios of the non-aquifer formations (Table 2) are generally higher and show less dispersion with depth than those of the Finlay Formation. The spreads in O and C isotope ratios of all Finlay wall-rock and vein samples are shown as box plots in Figure 3 in the general order of increasing distance from CM12-431. CM12-431 has been chosen as the point of "origin" due to the presence of strong mineralization surrounded by hundreds of meters of pervasive marble, hornfels, and skarn alteration indicating proximity to the likely heat and fluid source. CM10-247 is situated in a different mineralization zone 4 km to the west (Pozo Seco zone) but is considerably altered and is therefore placed to the left of CM12-431 in Figure 3.

Wall-rock local stable isotope background

The local stable isotope background is defined as the composition of hole CM09-94 in the southeast part of the Cinco the Mayo property. The distance of CM09-94 to the Upper

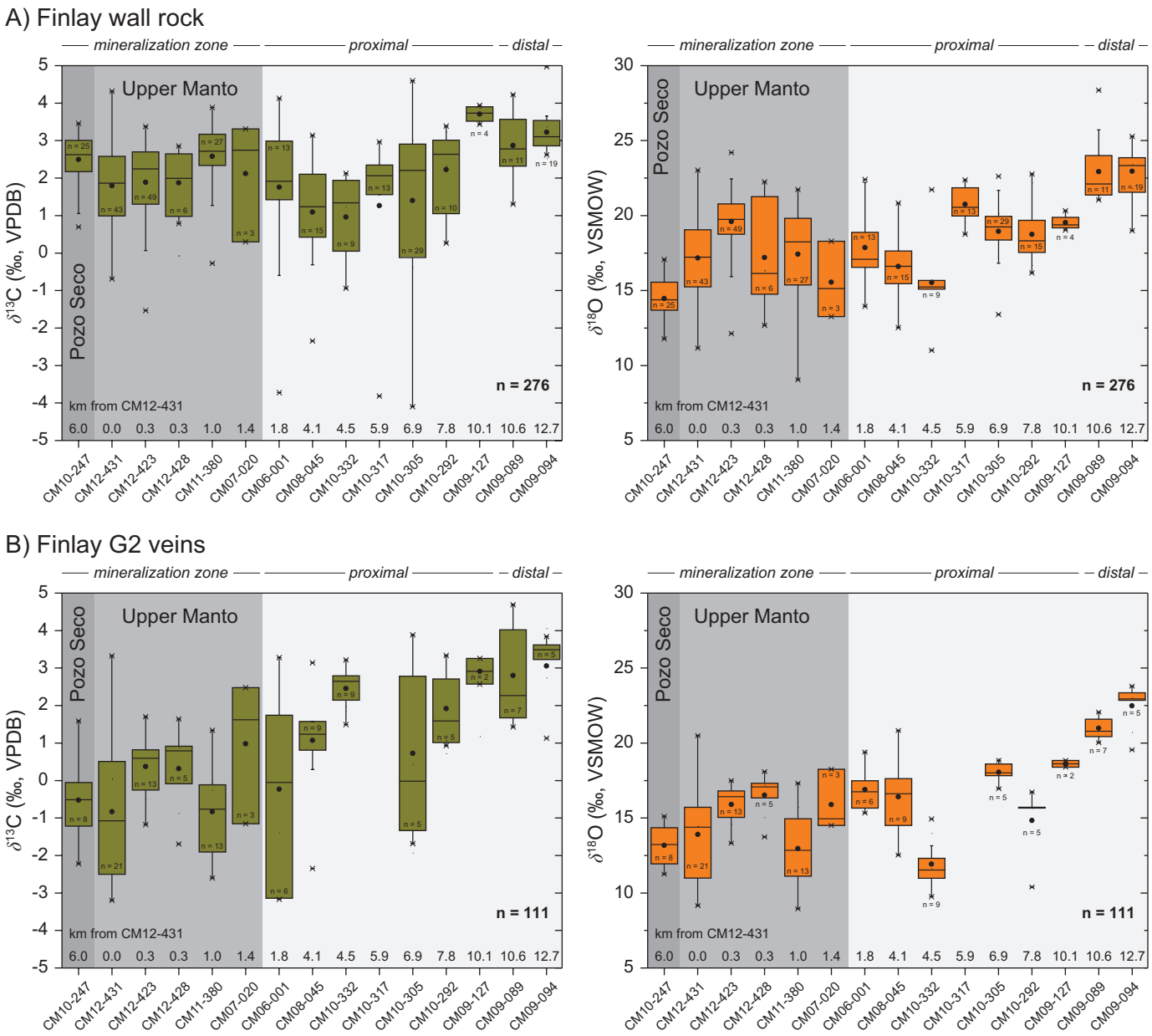

Fig. 3. Box plots for Finlay Formation (A) limestone wall rock and (B) G2 veins plotted in the order of increasing distance from CM12-431. CM12-431 was chosen as the origin based on the presence of hornfels, skarn, and strong mineralization. CM10-247 intersects the Pozo Seco zone mineralization and is plotted to the left of CM12-431. The span of the boxes represents the composition of 50% of the data population (interquartile range), the band within the box represents the median and the dot is the mean. The whisker length is 1.5 times the interquartile range; crosses define the 1 and 99% interval.

Manto is ~12.7 km. CM09-94 intersects the Finlay, Lagrima, Benigno, and Cuchillo Formations, all of which have constant $\delta^{13}C$ and $\delta^{18}O$ values throughout the entire length of the core (Fig. 2A). Averaged wall-rock $\delta^{13}C$ and $\delta^{18}O$ values are 3.1 ± 0.7 and 22.4 ± 1.7‰, respectively (n = 72). The composition of the Finlay limestone in CM09-94 is shown in Figure 3A (Table 3).

Wall rock in distal and proximal drill holes

The distal and proximal drill holes show average $\delta^{13}C$ and $\delta^{18}O$ values slightly below the local stable isotope background defined by CM09-94. The variations of isotope ratios with depth in these holes are more pronounced than in CM09-94. CM10-305 and CM10-292 are mostly within the Finlay Formation, CM09-127 intersects the Benavides, Finlay, Lagrima, and Benigno Formations and CM09-88 cuts just the Benigno and Cuchillo Formations. CM08-45 and CM10-332 are located ~3 km to the northwest and west from the Upper Manto, respectively. Samples from these two drill holes are from the Finlay Formation and are significantly depleted in ^{18}O and slightly depleted in ^{13}C relative to the local background. CM06-01 is located directly to the southwest of the Upper Manto. The average Finlay wall-rock $\delta^{13}C$ values for proximal samples vary between 0.9 ± 1.2 and 2.7 ± 0.8‰,

$\delta^{18}O$ values vary between 15.5 ± 2.9 and 20.8 ± 1.3‰ (Fig. 3A; Table 3).

Wall rock in mineralization zone samples

Most of the investigated mineralization zone holes intersect the Upper Manto with one additional hole from the Pozo Seco zone. Mineralization zone samples are characterized by highly variable isotope ratios with variations of up to 10‰ for both oxygen and carbon over depth intervals of 10 m or less (Fig. 2B). Average stable isotope ratios (shown as the 5-point moving average in Fig. 2) are significantly shifted to lower values compared to the local stable isotope background and proximal samples. CM12-431 intersects three mineralized zones where carbonate has been completely replaced by massive sulfide on the meter to tens of meters scale. The contact between massive sulfide and limestone host rock in CM12-431 is often characterized by meter-wide zones of white recrystallized calcite. Samples from these contact zones display the most depleted values, to as low as $\delta^{13}C$ = –6‰ and $\delta^{18}O$ = 10‰.

The depth interval with the strongest variation and lowest average stable isotope ratios coincides with intervals having high metal (e.g., Ag in Fig. 2B) and S concentrations within CM12-431 and CM12-423. Even though stable isotope alteration is preferentially developed in the Finlay Formation, it extends into the underlying Lagrima shale and Benigno limestone (Fig. 2B). Samples from the stratigraphically higher Benavides shale are often characterized by low carbonate mineral abundance and only a small number of samples could be analyzed owing to the lack of carbonate minerals. Average stable isotope ratios of Finlay limestone in CM12-431 and CM12-423 are $\delta^{13}C$ = 1.8 ± 1.2‰ (n = 43), 1.9 ± 1.2‰ (n = 90) and $\delta^{18}O$ = 17.2 ± 2.7‰ and 19.6 ± 2.2‰, respectively (Fig. 3A; Table 3). The isotope ratios gradually increase with depth and approach values identical to the local stable isotope background. This transition zone has a thickness of ~200 m in both drill holes (Fig. 2B; only shown for CM12-431). CM10-247 from Pozo Seco intersects the Finlay, Lagrima, Benigno, and Cuchillo Formations. The isotope ratios are consistently offset to lower values throughout the entire core and do not increase at depth (Tables 2, 3). The average Finlay wall-rock $\delta^{13}C$ is 2.5 ± 0.7‰ and $\delta^{18}O$ is 14.5 ± 1.3‰ (Figs. 2, 3).

Vein generations

Three generations of carbonate veins could be distinguished at Cinco de Mayo based on macroscopic textural observations and UV fluorescence. Throughout the following text, the different vein generations are referred to as G1, G2, and G3 veins with G1 being the first (oldest) and G3 the last (youngest) generation.

Generation 1 veins: The first vein generation displays a white color under normal light and appears boudinaged and/or folded on hand specimen scale. Interfaces between G1 veins and their wall rocks are typically diffuse. G1 veins do not crosscut stylolites and are crosscut by later, texturally distinct, vein generations G2 and G3 (Fig. 4A-C). Based on hand specimen observations and handheld X-ray fluorescence (XRF) analyses (data not shown), G1 veins are pure calcite and sulfide minerals have not been found in this vein type. The majority of veins showing these textural features are generally UV inactive but a very weak pink fluorescence was locally observed (Fig. 4A).

Generation 2 veins: On hand specimen scale, G2 veins are either straight or show evidence of brittle deformation. Interfaces with the surrounding wall rock are always sharp. G2 veins usually show a strong pink, or sometimes a blue UV fluorescence color and are rarely UV inactive (Fig. 4B-F). Where crosscutting relationships are evident, G2 veins are consistently younger than G1 veins and stylolites (Fig. 4B, D). Heavily veined samples sometimes exhibit mutual crosscutting relationships of veins consistent with the textural characteristics of G2 veins (Fig. 4F). These crosscutting G2 veins have been arbitrarily classified as vein types G2a and G2b with G2b veins being younger. G2 veins frequently contain sulfide minerals and display rusty discoloration spots, suggesting elevated Fe concentration and/or ankerite in addition to calcite.

Generation 3 veins: This third vein generation is distinguished based on textural relationships with sulfide minerals. While G2 veins are frequently sulfide bearing, G3 veins crosscut sulfide minerals and zones of massive sulfide mineralization. G3 veins are undeformed and sometimes show a weak pink UV fluorescence color (Fig. 4G, F). Interfaces with the surrounding sulfide host mineral are sharp and ankerite has not been detected in G3 veins. However, the absence of crosscutting relationships means textural classification criteria alone are insufficient to distinguish G2 and G3 veins outside of mineralized zones.

Vein carbonate stable isotope ratios

The stable isotope ratios of all analyzed calcite veins and their classification into the three vein generations are shown in Figure 5. The downhole distribution of vein calcite stable isotope ratios is shown for cores CM12-431 and CM09-94 in Figure 2. G1 veins show a wide spread of positively correlated $\delta^{13}C$ and $\delta^{18}O$ values ranging from –4 to 3‰ and 15 to 22‰, respectively (Fig. 5). G2 veins show a similar spread in $\delta^{13}C$ values between –3 and 4‰, while $\delta^{18}O$ values vary between 10 and 18‰. The compositional ranges of the two vein generations overlap but cluster in distinct areas on a $\delta^{18}O$ vs. $\delta^{13}C$ plot (Fig. 5). The stable isotope composition of G2b veins overlaps with that of G2a veins and ranges in $\delta^{13}C$ between 1.5 and 2.5‰ and in $\delta^{18}O$ between 14 and 19‰ (Fig. 5). G3 veins have a distinct stable isotope composition that is strongly depleted in both ^{13}C and ^{18}O relative to G1 and G2 veins. $\delta^{13}C$ values vary between –3 and –1‰, $\delta^{18}O$ between 8 and 13‰ (Fig. 5). The isotopically distinct composition of G3 and G2b veins supports their classification as separate generations. The compositional overlap of G3 veins with depleted G2a veins complicates their classification and a definitive classification is not always possible. Isotope ratios of G2 veins hosted in Finlay limestone are shown as box plots in Figure 3B.

Vein carbonate trace-element concentrations

Vein carbonate trace-element concentrations were measured on representative samples of the three vein generations and from the mineralization zone, proximal and distal cores. Concentrations were measured for Mg, Si, P, S, Mn, Fe, Cu, Zn, As, Sr, Y, Ba, Hf, Tl, Pb, Th, U, and rare earth elements (REE).

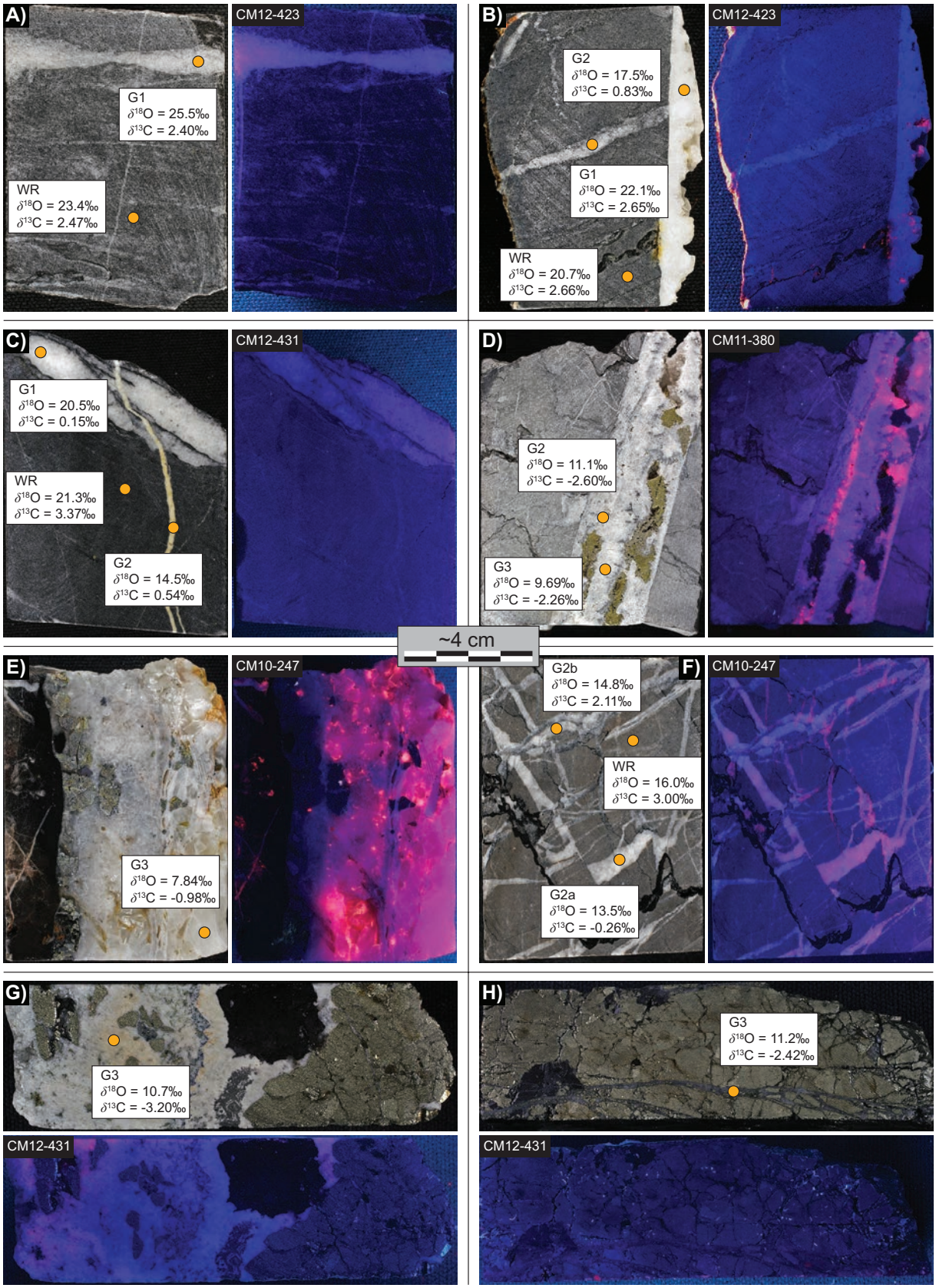

Fig. 4. Mosaic showing representative normal and UV light images of the different vein generations in half-core samples together with measured O and C isotope ratios. Note the yellow color of vein carbonate in G2 veins in CM12-431 indicating the presence of Fe and/or ankerite.

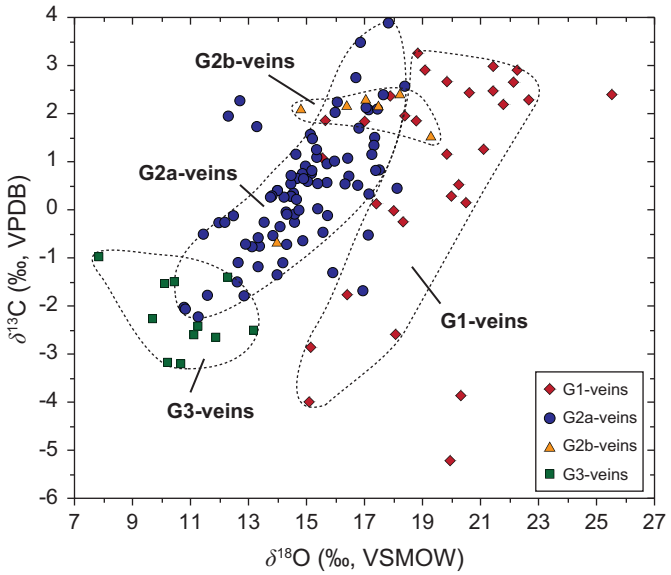

Fig. 5. $\delta^{13}C$ vs $\delta^{18}O$ data of the different calcite vein generations at Cinco de Mayo. Vein classification is based only on macroscopic textural observations but is consistent with distinct stable isotope compositions. Classification of G2a and G2b veins is based on crosscutting relationships between veins that are both texturally consistent with generation 2 veins. G2b veins are always younger than G2a veins.

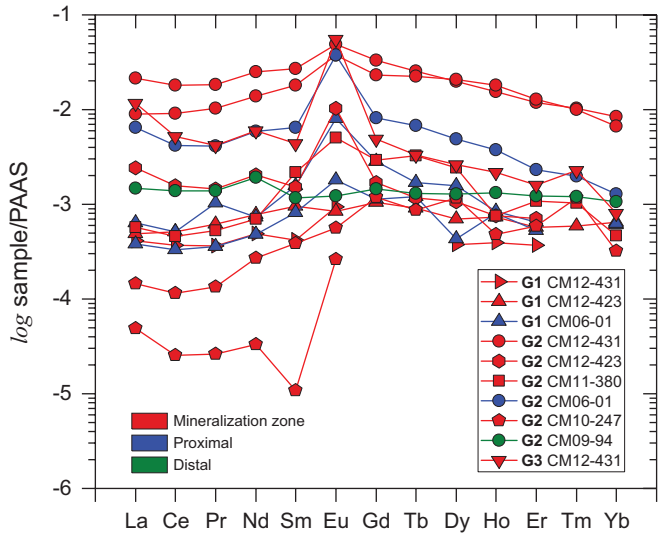

Fig. 6. Post-Archean Australian Shale (PAAS)-normalized vein calcite REE pattern from the three vein generations in mineralization zone, proximal, and distal samples. REE concentrations are average values calculated from the concentration of several laser ablation spots in each vein type per sample.

Generally, trace-element concentrations are low except those of Si, Mg, Fe, and Mn (435–4,050 ppm). Sulfur and Sr concentrations range between 30 and 10 ppm, concentrations of all other analyzed elements are below 10 ppm and mostly also below 1 ppm. In most samples P, Hf, Tl, and Th are below detection limits. Likewise, the heavy REE (HREE) Tm and Yb are generally near or below their detection limits (~0.03 ppb). Average trace-element concentrations on a per-vein basis are summarized in Table 4.

Systematic trace-element concentration differences exist between the different vein generations. The average concentrations of all analyzed trace elements are enriched in G2 veins and one analyzed G3 vein relative to G1 veins except Sr, which has similar concentrations in all three vein generations. The strongest enrichment (>10 times enriched) in average concentrations in G2 relative to G1 veins is found for Mn, Fe, Y, and REE. Mg, Cu, Zn, Pr, Sm, Ho, and Er are moderately enriched (5–10 times), while the remaining trace elements show a slight (<5 times) enrichment. Trace-element concentrations in the analyzed G3 vein are on average lower than in G2 veins. However, the G3 vein concentration of S, As, Sr, La, Ce, Eu, and Pb are weakly (<2.7 times) enriched or similar compared to G2 veins (Table 4). In addition, there is an observable enrichment trend in veins from distal through proximal to mineralization zone samples. The highest vein calcite trace-element concentrations are found in G2 veins in CM12-431.

REE concentrations normalized to Post-Archean Australian Shale (PAAS; McLennan, 1989) show relatively similar values for light REE (LREE) and HREE, while in some veins Eu and sometimes also the neighboring REE show a relative enrichment (Fig. 6). This enrichment is not systematic with respect to vein generation and distance to the mineralization zone. In contrast, absolute REE concentrations show systematic variations with respect to the vein paragenesis and distance from the mineralization zone. G2 veins from the mineralization zone show the highest REE concentrations and G2 veins are always enriched relative to G1 veins. However, REE concentrations in G2 veins from the Pozo Seco zone mineralization (CM10-247) are similar to G1 veins from the Upper Manto mineralization and proximal and distal G2 veins, but are lower than most Upper Manto G2 veins (Fig. 7). The variation of trace-element concentrations and ratios with distance from mineralization and vein calcite $\delta^{18}O$ is shown in Figure 8.

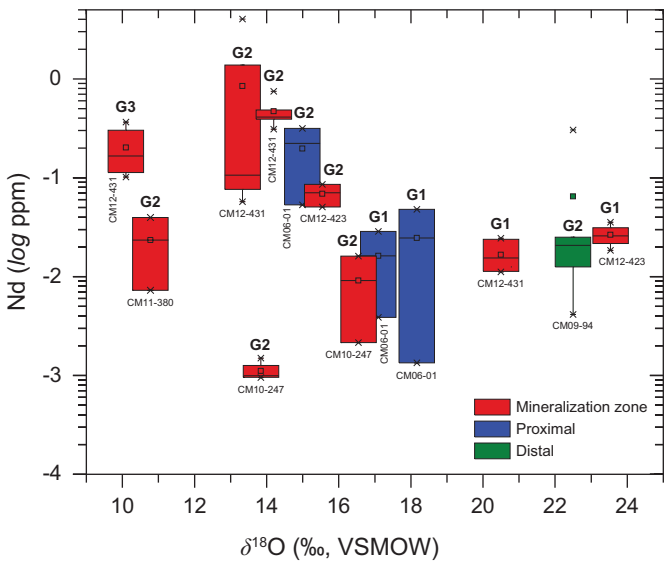

Fig. 7. Vein calcite Nd concentrations plotted against $\delta^{18}O$ for the three vein generations in mineralization zone, proximal, and distal samples. The spread in Nd concentrations reflects the per-vein compositional heterogeneity.

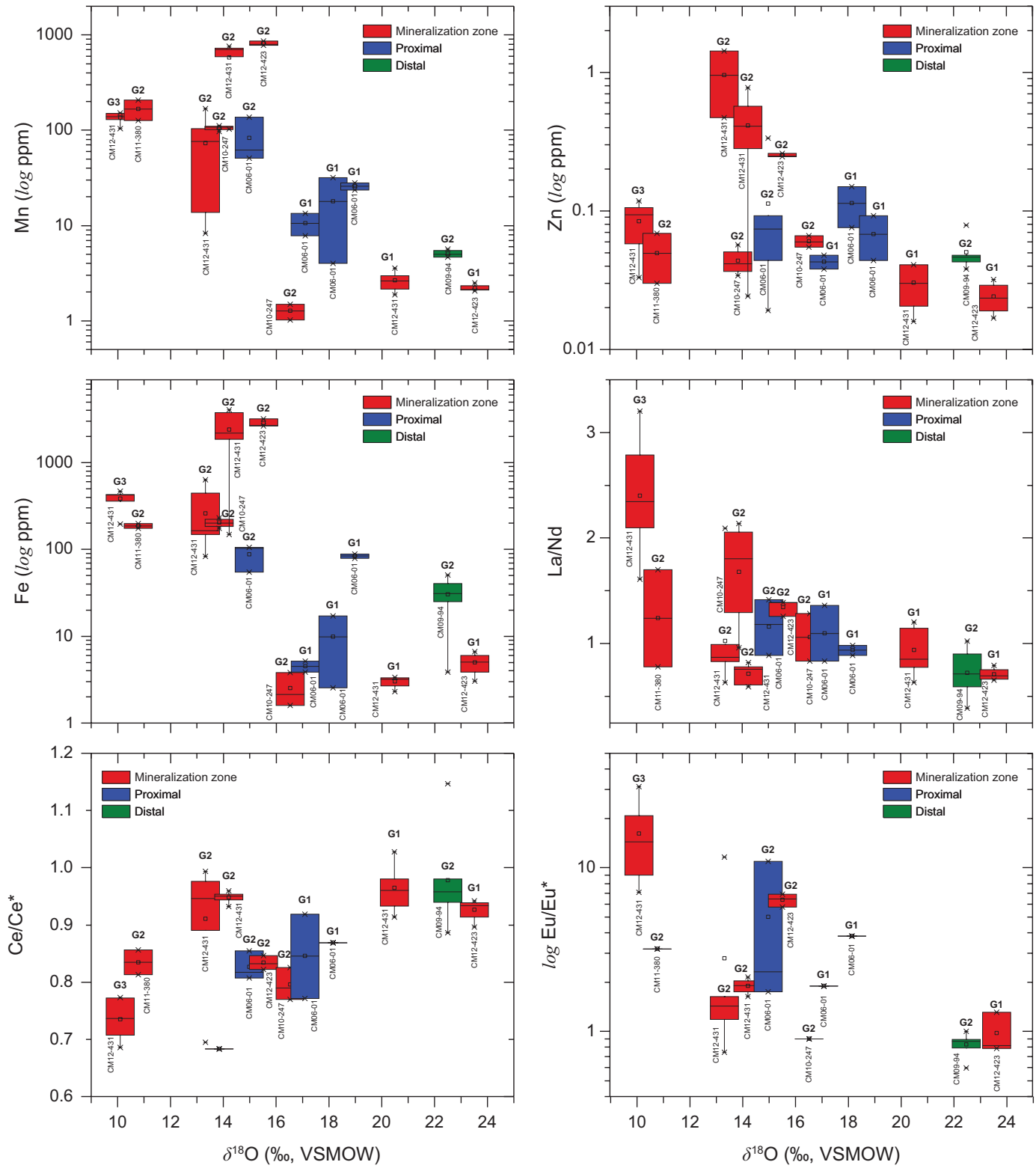

Fig. 8. Box plots showing the spread in selected trace metal concentrations and ratios plotted against vein calcite $\delta^{18}O$ for the three vein generations in mineralization zone, proximal, and distal veins. Ce/Ce* Eu/Eu* are PAAS-normalized (McLennan, 1989) concentrations divided by their predicted PAAS-normalized concentrations (Towell et al., 1965).

Table 4. Average Trace-Element Concentrations in Finlay Calcite Veins from the Mineralization Zone, Proximal, and Distal Holes Together with Their Stable Isotope Composition

Hole ID	CM09-94		CM11-380		CM06-01		CM06-01		CM06-01		CM06-01		JM12-423	
Vein type	G2		G2		G1		G1		G2		G2		G1	
$\delta^{13}C$ (‰)	3.1 ± 1.1		–2.0 ± 0.5		2.6 ± 0.8		2.1 ± 0.8		1.4 ± 0.8		–1.4 ± 0.8		1.64 ± 0.8	
$\delta^{18}O$ (‰)	22.5 ± 1.7		10.8 ± 0.7		17.1 ± 0.2		18.2 ± 0.1		19.0 ± 0.1		15.0 ± 0.1		23.5 ± 0.1	
n	6		2		2		2		2		3		4	
	avg ppm	s.d.	avg ppm	s.d.	avg ppm	s.d.	avg ppm	s.d.	avg ppm	s.d.	avg ppm	s.d.	avg ppm	s.d.
Mg	33.3	9.15	78.6	45.4	31.3	1.28	37.0	0.877	32.0	5.30	28.0	10.5	163	12.4
Si	14.5	2.38	13.2	2.40	15.5	0.495	12.8	1.13	12.3	0.283	28.5	22.1	9.70	1.28
P	0.220	b.d.l.	b.d.l.	b.d.l.	b.d.l.	b.d.l.	b.d.l.	b.d.l.	0.670	0.255	0.362	b.d.l.	b.d.l.	b.d.l.
S	1.96	0.204	4.00	0.297	2.73	0.417	2.57	0.148	27.1	2.41	8.32	5.49	3.33	0.430
Mn	5.06	0.424	167	57.9	10.6	3.96	17.9	19.7	25.8	3.16	82.9	46.6	2.21	0.196
Fe	30.4	15.8	187	16.0	4.52	0.905	9.85	10.4	83.8	7.00	87.8	28.3	4.94	1.50
Cu	0.008	0.009	0.002	0.000	0.004	0.001	0.003	b.d.l.	0.018	b.d.l.	0.005	0.003	0.005	0.003
Zn	0.050	0.015	0.050	0.028	0.043	0.007	0.113	0.052	0.068	0.034	0.143	0.169	0.024	0.007
As	0.017	0.012	0.012	0.001	0.015	0.006	0.011	0.002	0.011	0.004	0.011	0.001	0.009	0.002
Sr	4.04	0.608	13.3	5.73	9.23	5.18	6.73	0.278	9.06	5.08	9.09	1.95	12.9	0.219
Y	0.039	0.005	0.037	0.047	0.013	0.013	0.016	0.021	0.010	0.002	0.129	0.054	0.020	0.007
Ba	0.016	0.004	0.022	0.008	0.028	0.010	0.022	0.012	0.013	0.014	0.268	0.418	0.010	0.002
La	0.056	0.108	0.022	0.013	0.015	0.013	0.024	0.033	b.d.l.	b.d.l.	0.246	0.175	0.019	0.005
Ce	0.110	0.208	0.036	0.031	0.026	0.027	0.041	0.053	b.d.l.	b.d.l.	0.334	0.225	0.041	0.010
Pr	0.012	0.022	0.005	0.005	0.003	0.003	0.009	b.d.l.	b.d.l.	b.d.l.	0.037	0.024	0.005	0.002
Nd	0.065	0.118	0.024	0.023	0.016	0.018	0.025	0.033	b.d.l.	b.d.l.	0.198	0.134	0.027	0.007
Sm	0.006	0.007	0.012	b.d.l.	0.005	b.d.l.	0.009	b.d.l.	b.d.l.	b.d.l.	0.036	0.023	0.005	0.002
Eu	0.001	0.001	0.005	0.005	0.002	0.000	0.009	b.d.l.	b.d.l.	b.d.l.	0.040	0.047	0.001	0.000
Gd	0.007	0.004	0.014	b.d.l.	0.005	b.d.l.	0.013	b.d.l.	b.d.l.	b.d.l.	0.038	0.024	0.005	0.002
Tb	0.001	0.000	0.003	b.d.l.	0.001	b.d.l.	0.001	b.d.l.	b.d.l.	b.d.l.	0.005	0.003	0.001	0.000
Dy	0.006	0.001	0.011	b.d.l.	0.002	0.002	0.007	b.d.l.	b.d.l.	b.d.l.	0.023	0.012	0.003	0.001
Ho	0.001	0.000	0.001	0.001	0.001	b.d.l.	0.001	b.d.l.	b.d.l.	b.d.l.	0.004	0.002	0.001	0.000
Er	0.003	0.001	0.003	b.d.l.	0.002	b.d.l.	0.002	b.d.l.	b.d.l.	b.d.l.	0.007	0.003	0.002	0.001
Tm	0.000	0.000	0.000	b.d.l.	b.d.l.	b.d.l.	b.d.l.	b.d.l.	b.d.l.	b.d.l.	0.001	0.000	0.000	0.000
Yb	0.003	0.000	0.001	b.d.l.	0.002	b.d.l.	0.002	b.d.l.	0.000	b.d.l.	0.004	0.002	0.002	b.d.l.
Hf	0.001	0.001	b.d.l.	b.d.l.	b.d.l.	b.d.l.	b.d.l.	b.d.l.	b.d.l.	b.d.l.	0.001	b.d.l.	b.d.l.	b.d.l.
Tl	b.d.l.	b.d.l.	b.d.l.	b.d.l.	b.d.l.	b.d.l.	b.d.l.	b.d.l.	b.d.l.	b.d.l.	b.d.l.	b.d.l.	b.d.l.	b.d.l.
Pb	0.002	0.001	0.016	0.007	0.005	0.000	0.008	0.006	0.003	0.002	0.048	0.069	0.025	0.024
Th	0.000	0.001	b.d.l.	b.d.l.	b.d.l.	b.d.l.	b.d.l.	b.d.l.	b.d.l.	b.d.l.	0.001	0.002	b.d.l.	b.d.l.
U	0.002	0.003	0.002	0.001	0.000	b.d.l.	0.000	0.000	0.001	b.d.l.	0.003	0.003	0.002	0.003

Table 4. *(Cont.)*

Hole ID	JM12-423		CM12-431		CM12-431		CM12-431		CM12-431		CM10-247		CM10-247	
Vein type	G2		G1		G2		G2		G3		G2		G2	
$\delta^{13}C$ (‰)	0.7 ± 0.8		0.1 ± 0.2		–0.6 ± 0.2		0.3 ± 0.2		–1.5 ± 0.1		1.8 ± 0.8		–0.5 ± 0.3	
$\delta^{18}O$ (‰)	15.5 ± 0.1		20.5 ± 0.4		13.3 ± 0.4		14.2 ± 0.4		10.1 ± 0.4		16.5 ± 0.1		13.8 ± 0.4	
n	3		7		7		5		6		3		4	
	avg ppm	s.d.	avg ppm	s.d.	avg ppm	s.d.	avg ppm	s.d.	avg ppm	s.d.	avg ppm	s.d.	avg ppm	s.d.
Mg	2356	200	81.8	7.63	79.5	74.8	1585	1026	182	65.6	41.0	7.41	56.1	9.25
Si	17.7	3.50	22.8	12.0	125	173	23.7	2.66	13.8	1.90	15.1	0.635	14.1	1.75
P	b.d.l.	b.d.l.	b.d.l.	b.d.l.	22.7	b.d.l.	b.d.l.	b.d.l.	b.d.l.	b.d.l.	0.298	0.027	b.d.l.	b.d.l.
S	3.68	0.171	2.34	0.932	3.85	3.26	1.51	0.214	5.84	1.11	3.87	1.64	2.13	0.084
Mn	813	44.4	2.66	0.559	72.5	54.5	576	272	136	17.5	1.27	0.235	106	6.47
Fe	2846	318	2.99	0.390	259	201	2394	1579	383	98.0	2.50	1.15	203	24.1
Cu	0.007	0.001	0.006	0.002	0.102	0.134	0.075	0.124	0.022	0.036	0.004	0.001	0.005	0.002
Zn	0.252	0.008	0.030	0.011	b.d.l.	b.d.l.	0.412	0.284	0.084	0.033	0.060	0.006	0.044	0.010
As	0.021	0.004	0.014	0.004	0.043	0.031	0.008	b.d.l.	0.030	0.013	0.013	0.003	0.008	0.001
Sr	9.14	0.320	11.9	0.623	10.6	2.18	8.68	2.16	12.0	0.584	9.95	3.38	7.73	0.230
Y	0.036	0.010	0.006	0.003	0.529	0.695	0.556	0.201	0.078	0.047	0.019	0.024	0.000	0.000
Ba	0.096	0.005	0.022	0.016	0.048	0.038	0.058	0.016	0.048	0.017	0.021	0.005	0.013	0.008
La	0.093	0.025	0.016	0.007	0.818	1.47	0.340	0.159	0.445	0.178	0.006	0.007	0.002	0.001
Ce	0.125	0.035	0.030	0.011	1.44	2.55	0.724	0.307	0.413	0.219	0.009	0.012	0.002	0.001
Pr	0.013	0.004	0.003	0.001	0.162	0.283	0.092	0.035	0.037	0.021	0.001	0.002	0.000	b.d.l.
Nd	0.069	0.018	0.017	0.006	0.852	1.49	0.472	0.170	0.204	0.112	0.009	0.010	0.001	0.000
Sm	0.008	0.001	0.002	0.001	0.151	0.265	0.100	0.031	0.025	0.016	0.002	0.002	0.000	0.000
Eu	0.011	0.002	0.001	0.000	0.053	0.091	0.041	0.010	0.060	0.013	0.001	0.000	0.000	0.000
Gd	0.008	0.002	b.d.l.	b.d.l.	0.155	0.270	0.108	0.041	0.023	0.016	0.006	b.d.l.	b.d.l.	b.d.l.
Tb	0.001	0.000	b.d.l.	b.d.l.	0.020	0.030	0.017	0.007	0.003	0.001	0.001	b.d.l.	b.d.l.	b.d.l.
Dy	0.005	0.001	0.002	0.001	0.093	0.121	0.097	0.036	0.012	0.008	0.006	b.d.l.	b.d.l.	b.d.l.
Ho	0.001	0.000	0.000	0.000	0.015	0.019	0.018	0.006	0.002	0.001	0.000	0.001	b.d.l.	b.d.l.
Er	0.002	0.000	0.001	b.d.l.	0.034	0.042	0.037	0.011	0.005	0.003	0.002	0.001	b.d.l.	b.d.l.
Tm	b.d.l.	b.d.l.	b.d.l.	b.d.l.	0.004	0.005	0.004	0.001	0.001	0.000	0.000	b.d.l.	b.d.l.	b.d.l.
Yb	b.d.l.	b.d.l.	b.d.l.	b.d.l.	0.024	0.032	0.019	0.004	0.002	0.002	0.001	b.d.l.	b.d.l.	b.d.l.
Hf	b.d.l.	b.d.l.	b.d.l.	b.d.l.	0.013	0.010	b.d.l.	b.d.l.	b.d.l.	b.d.l.	0.001	0.000	0.000	b.d.l.
Tl	b.d.l.	b.d.l.	0.002	0.001	0.001	0.001	b.d.l.	b.d.l.	b.d.l.	b.d.l.	b.d.l.	b.d.l.	b.d.l.	b.d.l.
Pb	0.017	0.006	0.010	0.001	0.044	0.043	0.025	0.006	0.023	0.004	0.003	0.000	0.016	0.000
Th	0.000	0.000	b.d.l.	b.d.l.	0.014	0.014	0.001	0.000	0.000	0.000	0.001	0.001	b.d.l.	b.d.l.
U	0.002	0.001	b.d.l.	b.d.l.	0.046	0.062	0.000	0.000	0.001	0.000	0.123	0.103	b.d.l.	b.d.l.

b.d.l. = below the detection limit; $\delta^{13}C$ relative to VPDB, $\delta^{18}O$ relative to VSMOW; the standard deviation (1σ) reflects the spread of the overall data population

Discussion

Correlation between the local, regional, and global stable isotope background

The least-altered drill hole at Cinco de Mayo (CM09-94) shows average isotope ratios for Finlay limestone of $\delta^{13}C$ = 3.3 ± 0.6‰ and $\delta^{18}O$ = 23.0 ± 1.5‰. In comparison, global scale C and O isotope ratios of Cretaceous limestone range between –5 and 5‰ for $\delta^{13}C$ and 23 and 30‰ for $\delta^{18}O$ (Veizer et al., 1999). While $\delta^{13}C$ values of the least-altered Finlay limestone are consistent with the global average ($\delta^{13}C$ = 2.4‰), $\delta^{18}O$ is depleted (global average $\delta^{18}O$ = 27.7‰). This shift in $\delta^{18}O$ values suggests isotope exchange on a scale larger than the alteration associated with mineralization at Cinco de Mayo, i.e., on a regional scale. Thus, using the local stable isotope background ($\delta^{18}O$ = 23.0 ± 1.5‰) allows for separating oxygen isotope compositional changes related to synmineralization fluid flow from that resulting from earlier alteration that is unrelated to mineralization. The appearance of G1 veins can be interpreted as to result from ductile deformation (folded, boudinaged) and/or partial recrystallization. Their $\delta^{18}O$ composition is similar to that of the least-altered limestone wall rock, suggesting that G1 vein formation is related to the regional scale shift in limestone $\delta^{18}O$ to ~23‰, which may have occurred during carbonate sediment diagenesis and compaction.

Megaw (1990) reported stable isotope ratios for barren Finlay limestone from the Santa Eulalia mining district, ~250 km to the south of Cinco de Mayo, that are –0.8‰ for $\delta^{13}C$ and 21.8‰ for $\delta^{18}O$. Sweeney (1987) reported $\delta^{13}C$ values of 1‰ and $\delta^{18}O$ values of 18‰ for unaltered Finlay limestone from the Naica district, ~350 km to the south of Cinco de Mayo. While there is general agreement between the three sites, stable isotope ratios of least-altered limestone from Cinco de Mayo are slightly higher than those from Santa Eulalia and Naica. The reason for these slight differences may simply reflect heterogeneous alteration during carbonate diagenesis or weak alteration of distal rocks during mineralization at Santa Eulalia and Naica. The least-altered Finlay samples used by Megaw (1990) to define the Santa Eulalia C and O isotope background were sampled at a distance of ~3 km from the mineralization zone. It can be speculated that this sample was exposed to distal stable isotope alteration despite the absence of visible mineralization given the size of previously documented ^{18}O alteration halos in carbonate rocks (Kesler et al., 1995; Vazquez et al., 1998; Barker et al., 2013). Additionally, the relatively low background $\delta^{18}O$ values reported from Naica (Sweeney, 1987) may also reflect distal alteration (Megaw, pers. commun.) and values between 25 and 27‰ were found in samples collected at ~3 km from the mine area (Kesler et al., 1995). Further sampling of regional rocks thought to be unaffected by hydrothermal alteration would be needed to confidently establish a regional vs. local background at Cinco de Mayo. Here, we assume that the local $\delta^{18}O$ background is ~23‰.

Constraints on the stable isotope composition and temperature of the mineralization fluid

The decrease of vein and wall-rock stable isotope ratios in the proximity to mineralization is consistent with isotope exchange reactions driven by reactive fluid that is enriched in the light isotope. The stable isotope composition of G2 vein calcite (frequently with sulfide minerals) from the mineralization zone can be taken as synchronous with sulfide precipitation and used to constrain the composition and source of the incoming mineralization fluid. G1 veins are likely related to diagenesis and G3 veins postdate mineralization and may represent late-stage fluid flow or be completely unrelated. The composition of G2 veins from the mineralization zone clusters around –1‰ for $\delta^{13}C$ and 13‰ for $\delta^{18}O$ (Figs. 2, 3, and 5) and this composition in combination with fluid-calcite O isotope fractionation factors can be used to constrain the stable isotope composition of the vein-forming and mineralizing fluid. However, the derived constraints are based on the assumption that isotopic equilibrium was attained during the alteration and are thus subject to uncertainty.

The mineralization temperature at Cinco de Mayo is unconstrained but a range of 250° to 500°C is accepted for most carbonate-hosted Ag-Pb-Zn-Cu deposits in northern Mexico (Haynes and Kesler, 1988; Megaw et al., 1988). Adopting this temperature range and suitable calcite-fluid O isotope fractionation factors (Chacko et al., 2001)2001 in combination with the measured O isotope ratio of vein calcite (~13‰) indicate an O isotope ratio of the alteration fluid between 5.7‰ (250°C) and 11.2‰ (500°C). If it is assumed that the infiltrating fluid was magmatic ($\delta^{18}O$ = 7–9‰; Taylor, 1974), then the observed vein calcite $\delta^{18}O$ values would be in equilibrium with magmatic fluid at temperatures between ~290° and ~360°C. Within the discussed uncertainties, the oxygen isotope composition of G2 vein calcite is therefore consistent with a dominantly magmatic source for the mineralizing fluid. A similar conclusion was reached for limestone alteration at Providencia, northern Mexico (Rye, 1966; Rye and O'Neil, 1968).

Fluid-flow model for isotope alteration

Hydrothermal limestone alteration proceeds as a dissolution-precipitation reaction allowing for isotope exchange between the solid and fluid. The alteration pervasiveness, the resulting shift in stable isotope composition, and the propagation distance of the alteration front from the fluid inlet depend on the fluid volume, the relative difference in solid and fluid compositions, temperature, rates of fluid-mineral isotope exchange, and the transport mechanism. A conceptual, one-dimensional reactive transport model for infiltration of magmatic fluid enriched in the light isotope into heavy isotope-enriched limestone is shown in Figure 9. This model is only an approximation because the one-dimensional flow vector cannot capture complex natural fluid dynamics resulting from heterogeneities in the aquifer permeability. Keeping these uncertainties in mind, the model provides a framework that allows relating the measured stable isotope composition of altered wall-rock and vein samples to the progressively changing isotopic composition of the reactive alteration fluid. Rates of fluid-mineral isotope exchange are related to transport rates using the dimensionless Damköhler number (N_D = reaction rate/transport rate). A high N_D ($N_D \geq$ ~10) indicates instantaneous reaction and transport limited reaction front propagation, whereas the isotope alteration front lags behind the fluid front at low N_D ($N_D < 1$). The dimensionless Peclet number describes the relative proportion of advective to diffusive isotope transport (N_{Pe} = advective transport rate/

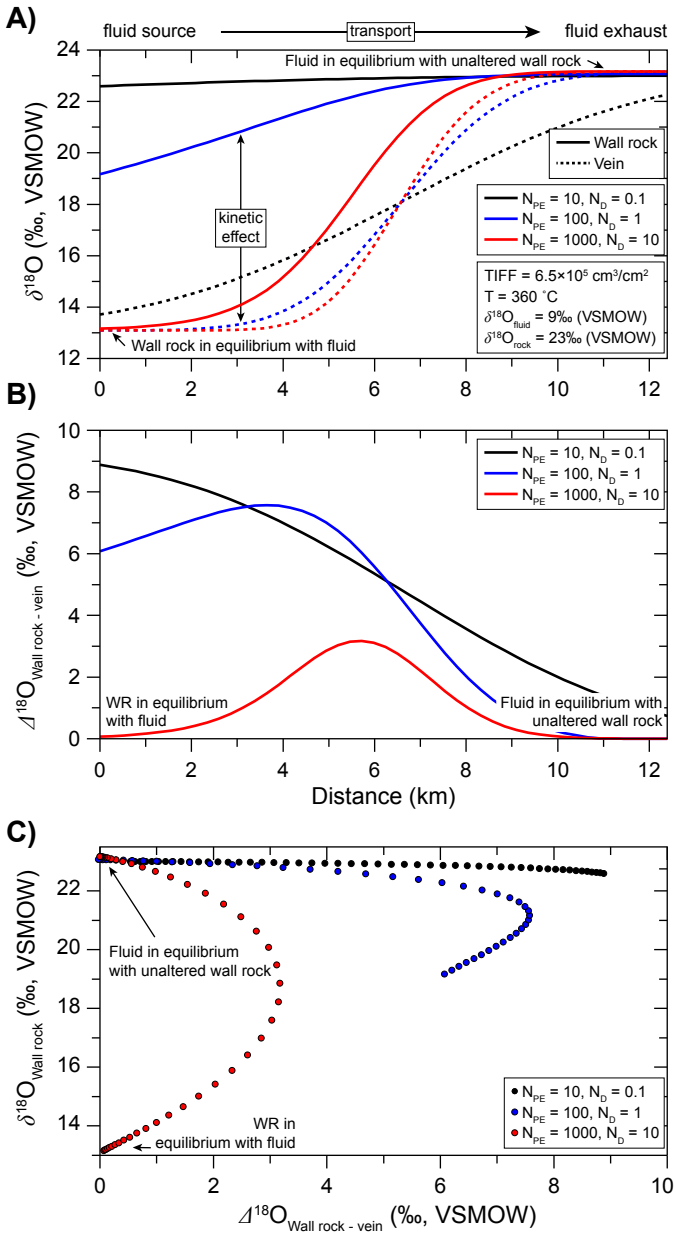

Fig. 9. Conceptual one-dimensional model of fluid flow and stable isotope alteration in limestone during infiltration of magmatic fluid. The composition of altered wall rock (solid lines) and coexisting veins (stippled lines) is shown for different Damköhler and Peclet numbers. The input fluid $\delta^{18}O$ composition (9‰) is consistent with a magmatic fluid, the initial wall-rock $\delta^{18}O$ composition represents the stable isotope background (23‰) in CM09-94. Fluid transport is from left to right. The fluid-calcite oxygen isotope fractionation factor (Chacko et al., 2001) is calculated for an assumed temperature of 360°C (see text for discussion). (A) Wall-rock and vein $\delta^{18}O$ composition as a function of distance from the fluid inlet, showing the shape of the alteration front in wall rock and vein samples for different fluid transport scenarios. (B) Compositional difference between wall rock and vein ($\Delta^{18}O_{WR\text{-}vein}$) for the fluid transport scenarios shown in (A) as a function of distance from the fluid inlet. (C) $\Delta^{18}O_{WR\text{-}vein}$ plotted against $\delta^{18}O_{WR}$ for the different cases shown in (A) and (B).

diffusive transport rate) and controls the sharpness of isotope ratio gradient along the flow path. The length scale of front propagation is a function of the total fluid volume involved in the alteration, expressed as time-integrated fluid flux (TIFF in cm^3/cm^2) reflecting the total fluid volume (cm^3) entering the aquifer per unit area (cm^2) at the fluid inlet. Details on the modeling approach can be found elsewhere (e.g., Lassey and Blattner, 1988; Dipple and Ferry, 1992a; Bowman et al., 1994; Knoop et al., 2002).

Wall rock and vein carbonate will assume similar stable isotope ratios ($\Delta^{18}O_{WR\text{-}vein} \approx 0$) near the fluid source due to pervasive wall-rock alteration and in distal parts of the system where the fluid composition approaches equilibrium with the limestone wall rock. The two locations where $\Delta^{18}O_{WR\text{-}vein} \approx 0$ are thus paired with low and high wall-rock $\delta^{18}O$, respectively (Fig. 9A, B). The position of the latter defines the limit of the stable isotope alteration footprint. In between the two "endpoints," sluggish reaction kinetics will produce vein calcite that is enriched in the light isotope relative to its moderately altered wall rock ($\Delta^{18}O_{WR\text{-}vein} > 0$). Scenarios for different values of N_{Pe} and N_D are shown in Figure 9.

The $\Delta^{18}O_{WR\text{-}vein}$ and $\delta^{18}O_{WR}$ values of distal, proximal, and mineralization zone samples (Fig. 10A) are consistent with the conceptual model (Fig. 9). Mineralization zone samples are characterized by low $\Delta^{18}O_{WR\text{-}vein}$ at low $\delta^{18}O_{WR}$, indicating proximity to the fluid inlet, whereas distal samples show low to intermediate $\Delta^{18}O_{WR\text{-}vein}$ values at high $\delta^{18}O_{WR}$. However, a number of samples display negative $\Delta^{18}O_{WR\text{-}vein}$ values and therefore appear inconsistent with the theory (Fig. 10A). Negative $\Delta^{18}O_{WR\text{-}vein}$ values may result from erroneous vein generation classification, or may represent a different snapshot of the same alteration event. Pulsed fluid supply and/or fracture healing and vein calcite formation at different times can form isotopically distinct veins that are all related to mineralization, thus representing the dynamically changing fluid composition during the alteration (see Bowman et al., 1994, for discussion). Continued wall-rock alteration may then result in the observed negative $\Delta^{18}O_{WR\text{-}vein}$ values. The majority of seemingly inconsistent vein–wall-rock pairs are from CM10-247 (Pozo Seco zone) and comprise strongly altered wall rock and less depleted G2 veins that are compositionally and texturally distinct from G1 veins. These samples are therefore indicative of early vein formation predating the final isotope alteration of the surrounding wall rock. This rationale also applies to samples from CM12-423 and CM12-431. Negative $\Delta^{18}O_{WR\text{-}vein}$ values from CM09-89 represent vein carbonate rich in the heavy isotope in slightly altered limestone wall rock. As for negative $\Delta^{18}O_{WR\text{-}vein}$ values from the mineralization zone, veins with high $\delta^{18}O$ in CM09-89 may represent an early stage of vein formation. Alternatively, the veins may be diagenetic G1 veins that show textural characteristics of G2 veins but are unlikely to be postmineralization since the composition of G3 veins is consistently low in ^{18}O (Fig. 5).

Vein–wall-rock pairs that appear to record the final alteration progress (i.e., positive $\Delta^{18}O_{WR\text{-}vein}$) allow for the evaluation of fluid volume and reaction kinetics and can thus aid in interpreting individual samples within the context of the larger scale hydrothermal system. Figure 10B shows vein–wall-rock pairs with $\Delta^{18}O_{WR\text{-}vein} > 0$ together with contours outlining Damköhler numbers and the TIFF-normalized distance (distance/TIFF) from the magmatic fluid inlet near hole CM12-431. The volume of fluid (TIFF) driving the isotope alteration front is approximately proportional to its propagation distance from the source (Hofmann, 1972). Hence, pervasively altered

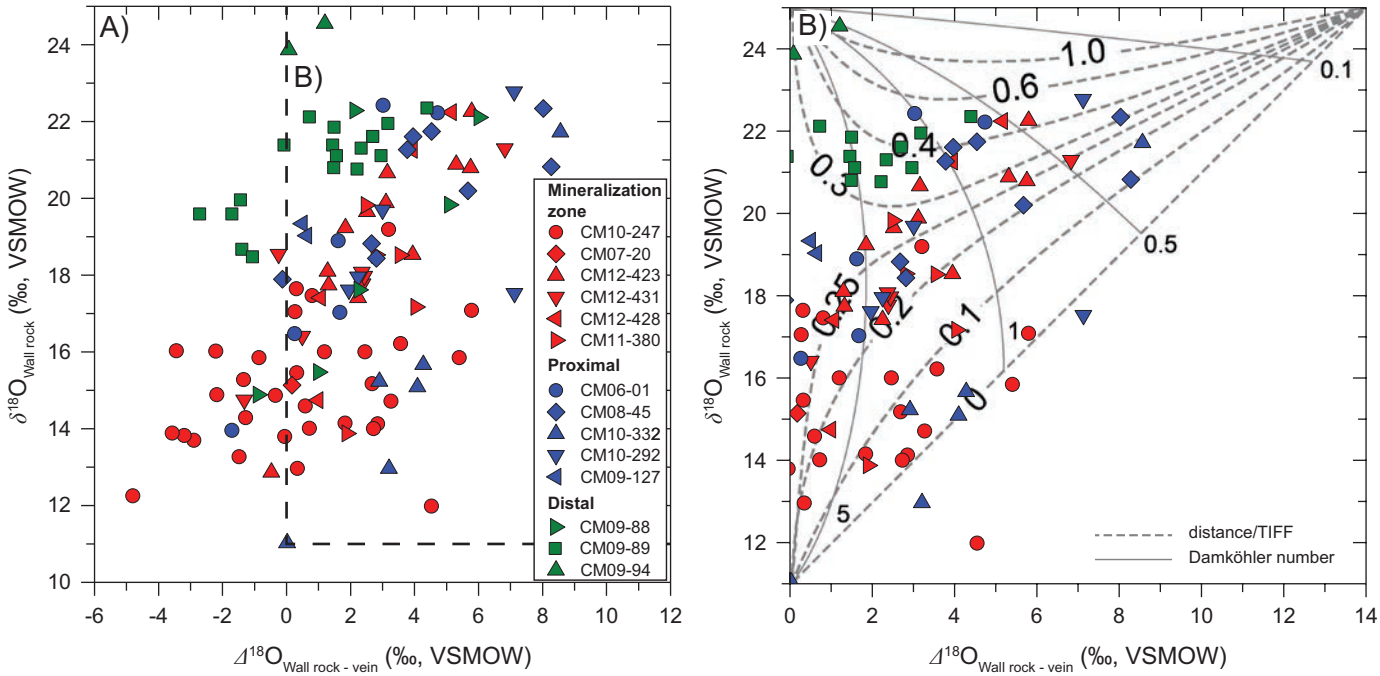

Fig. 10. $\Delta^{18}O_{WR\text{-}vein}$ vs. $\delta^{18}O_{WR}$ values of mineralization zone, proximal, and distal samples. (A) All data including negative $\Delta^{18}O_{WR\text{-}vein}$ values representing incomplete wall-rock alteration (see text for discussion). (B) $\Delta^{18}O_{WR\text{-}vein}$ vs. $\delta^{18}O_{WR}$ pairs shown for $\Delta^{18}O_{WR\text{-}vein} > 0$ using G2 veins from the Finlay Formation only. The contour lines represent distance normalized to the time-integrated fluid flux (stippled lines; z/TIFF) and Damköhler numbers (solid lines; N_D). Compare with Figure 9C for the construction of the contour lines.

mineralization zone samples plot at low z/TIFF values, whereas moderately altered proximal and distal samples plot at higher z/TIFF values. Figure 10B can be used to approximate the TIFF if the distance of the sample to the assumed fluid inlet is known. For example, $\Delta^{18}O_{WR\text{-}vein}$ and $\delta^{18}O_{WR}$ values of CM09-89 (z = ~10.6 km) plot between 0.3 and 0.5 (Fig. 10B) suggesting a TIFF of 2.1×10^6 to 3.5×10^6 cm^3/cm^2. Flux estimates based on the composition and location of CM10-292 and CM08-45 yield similar results. This estimate is consistent with crustal fluid flux during regional metasomatism and contact metamorphism (Ferry and Dipple, 1991; Dipple and Ferry, 1992b; Ague, 1997), including carbonate-hosted systems (Ferry et al., 2002). Furthermore, the position of $\Delta^{18}O_{WR\text{-}vein}$ vs. $\delta^{18}O_{WR}$ pairs in Figure 10B reflects the rate of isotope exchange reactions between the fluid and wall rock along flow through the aquifer. Fast reactions result in $\Delta^{18}O_{WR\text{-}vein}$ vs. $\delta^{18}O_{WR}$ pairs plotting at high N_D, while sluggish reactions plot at low N_D (Fig. 10B). Figure 10B therefore indicates changing reaction kinetics from fast within the mineralization zone to sluggish in distal parts of the system, potentially related to fluid cooling along its flow path.

In summary, the measured oxygen isotope composition of Cinco de Mayo wall-rock and vein calcite samples is consistent with a simple one-dimensional fluid flow and alteration model (Fig. 11A, B). CM09-94 represents the least-altered background based on only a small isotope ratio dispersion with depth, similar vein and wall-rock compositions, and the high wall-rock O isotope ratios. In most cases, proximal and mineralization zone samples show isotopically depleted veins and relatively strong variations of depleted wall-rock O isotope values. The compositional variations between veins and wall rocks indicates that close to equilibrium conditions have been reached locally (Fig. 10B); consistent with the presence of preferential fluid pathways. CM09-89 represents the most distal part of the system where stable isotope alteration is detectable and thus defines the extent of the stable isotope alteration footprint at ~11 km from the mineralization zone (Fig. 11A, B). The large size of this ^{18}O depletion halo may be explained by the presence of a large fluid-flow system requiring pore space connectivity on the km scale or fluid infiltration into the Finlay Formation at multiple, potentially structurally controlled, fluid inlets. However, the outlined consistency of the distribution of isotopic alteration with a simple one-dimensional flow system and the concentrated occurrence of hornfels alteration and mineralization indicative of a localized heat and fluid source imply that large-scale limestone stable isotope alteration at Cinco de Mayo was facilitated by overall fluid connectivity facilitated by the presence of the storm rip-up clast horizon and paleokarst in the upper Finlay Formation.

Correlation of vein calcite trace-element concentrations with stable isotope ratios

The inverse correlation of vein calcite trace-element concentrations with respective O isotope ratios corroborates the link between mineral deposit formation and limestone stable isotope alteration. This correlation is most strongly developed for Zn, Mn, As, Fe, Y, and Pb concentrations. For some samples this correlation seems less clear than for others, which may be related to the different sample volume used during carbonate stable isotope analysis compared to the volume of laser ablation spots during trace-element analysis. Despite considerable

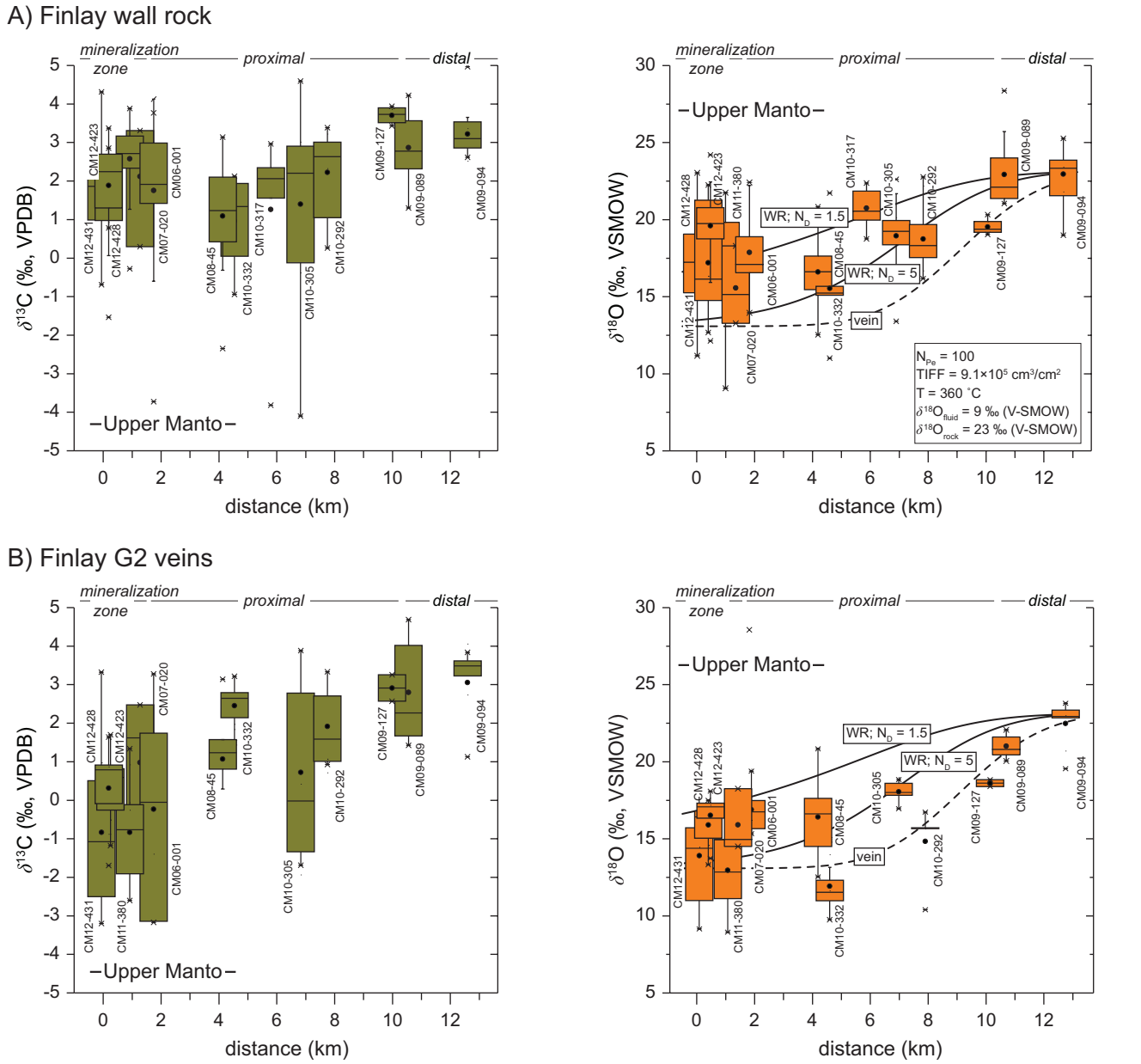

Fig. 11. Box plot showing the $\delta^{18}O$ and $\delta^{13}C$ composition of (A) Finlay wall rock and (B) vein samples plotted as function of distance from CM12-431. The solid (wall rock) and stippled (vein) lines in $\delta^{18}O$ plots represent the best fit of the real data to the one-dimensional transport model shown in Figure 9 using advection dominated fluid flow (N_{Pe} = 100) and Damköhler numbers of 1.5 and 5.

spread even on the per-vein basis, trace-element concentrations in mineralization zone G2 veins from cores CM12-431 (and sometimes also CM12-423) are typically two orders of magnitude higher than in G1 veins and distal G2 veins. However, mineralization zone hole CM11-380 shows both low $\delta^{18}O_{vein}$ and trace-element concentrations, which may be related to metal deposition from the fluid prior to vein calcite precipitation (Fig. 8; Table 4). Trace-element enrichment in G2 veins, particularly within the mineralization zone, is consistent with their strong fluorescence under UV light. Manganese substitution is a common cause of fluorescence in carbonates together with other activators including REEs, Zn, and lattice defects (Schulman et al., 1947; Gies, 1975). The high Fe concentration in G2 calcite veins is consistent with the presence of additional ankerite in some of the G2 veins (Table 4).

REE concentrations and their ratios, including PAAS-normalized (McLennan, 1989) Ce/Ce* and Eu/Eu*, appear to vary non-systematically with position along the hydrothermal flow path, vein generation, and $\delta^{18}O_{vein}$ (Fig. 8). However, the G3 vein in CM12-431 shows significantly elevated La/Nd, La/Yb, Eu/Eu*, and low Ce/Ce* compared to all other analyzed veins. This vein has also the lowest $\delta^{18}O$ value, which corroborates the distinction of G3 veins as individual group. Figure 6 shows that a positive Eu-anomaly has preferentially developed in G2 veins relative to G1 veins from the same hole. For example, G1 veins from CM12-431, CM12-423, and CM06-01 show no

or only a weak Eu-anomaly, whereas G2 veins from these holes show a distinct Eu-anomaly with the exception of one G2 vein in CM12-423 (Fig. 6). Generally, the relatively flat REE pattern of vein calcite may result from the presence of excess Ca^{2+} relative to CO_3^{2-} in the alteration fluid. Calcite preferentially incorporates Eu^{3+} and the Eu-anomaly present in only some of the G2 veins may indicate their formation prior to G2 veins lacking the Eu-anomaly, which may be related to cooling-induced reduction of Eu^{3+} and/or decreased ligand concentrations (CO_3^{2-}, HCO_3^-, F^-) (Bau, 1991). The relatively low Ce/Ce^* (~0.75) in G3 vein calcite from CM12-431 suggests reducing conditions of late-stage fluid, which may be unrelated to mineralization but is consistent with cooling of the system during or after mineralization (Bau and Möller, 1992). High metal concentrations in the G3 vein (Fig. 8A, B) may reflect incorporation of remobilized metal from the sulfide wall rock during postmineralization fluid flow.

Implications and application of carbon and oxygen isotopes to mineral exploration

Detailed analysis of vein samples and vein–wall-rock pairs appear to have promise for mineral deposit vectoring. The offset between the global isotopic reference frame and the inferred least altered samples at Cinco de Mayo and other deposits (cf. Santa Eulalia, Naica, Providencia) underscores the need during mineral exploration stable isotope programs for defining the local background against which mineralization-related changes in stable isotope ratios can be compared. Relative to global values, the least-altered samples may appear strongly altered but that shift in stable isotope ratios is likely unrelated to mineralization and therefore may be misleading. This can be achieved by taking several tens of samples per limestone unit at progressive distances sufficiently far away from the assumed center of mineralization (>10 km) to avoid distal intrusion-related alteration. Once the extent of the isotope alteration halo is established, preferential fluid-flow paths can be delineated by systematic high-resolution sampling at ~5- to 10-m-depth intervals of 1 to 3 complete drill holes from within the alteration halo. Additional sampling may then target vein–wall-rock pairs from the aquifer every 2 to 3 km at coarser spacing of ~10 pairs per drill hole, depending on aquifer thickness. These will reveal isotopic gradients that vector toward mineralization and reflect the alteration intensity and fluid volumes involved (Fig. 10). Large ore deposits are unlikely to form from small fluid volumes, so constraining the volume of alteration fluids is important because large-scale pervasive isotope alteration requires a large fluid flux, which in turn increases the likelihood for larger volumes of contained metal (Waring et al., 1998). Oxygen isotope ratios and particularly those of vein carbonate show stronger gradients between mineralization zone and unaltered distal rocks and will therefore provide a clearer signal of this mineralization-related fluid flow (Fig. 11).

Classification of different vein generations based only on textural observations aided by UV fluorescence studies is time-efficient and provides an independent tool to distinguish significant from unimportant and unrelated veins. Vein carbonate stable isotope ratios can be combined with trace-element analysis (As, Fe, Mn, Zn, La, Ce, Pr, Sm, Eu, Gd) of select samples to evaluate different vein types for their metal concentrations and constrain redox conditions of the vein-forming fluid. In addition, it is possible that portable XRF analysis of carbonate veins may be useful to help further characterize carbonate vein chemistry (Andrew and Barker, 2017) and aid in identifying and discriminating vein generations. The method of isotopic analysis employed here, incorporating sampling using a handheld drill followed by laser spectrometry analysis, represents an adequate approach to achieve the required sample throughput rate in mineral exploration programs. The robustness and simple operation of available ICOS isotope analyzers are beneficial for this application and allow real-time stable isotope analyses during core logging on site. Indeed, the low power and consumable requirements mean that the analytical setup utilized for this study could be easily deployed in a core shed (or even in a fly camp) setting if needed for rapid data generation.

Conclusions

Formation of the Cinco de Mayo Zn-Ag deposit was accompanied by extensive stable isotope alteration of the host limestone formations. This alteration is best developed in the middle Albian Finlay Formation, which was the major aquifer for the hydrothermal mineralization fluid. The stable isotope composition of pervasively altered holes intersecting the Upper Manto mineralization indicates hydrothermal fluid flow also crossed formation boundaries for ~200 m into the underlying Lagrima and Benigno Formations. Hydrothermal limestone alteration resulted in an overall shift of average wall-rock stable isotope ratios to values lower than in the least altered distal hole (CM09-94) as well as strongly erratic stable isotope ratios of individual samples that vary up to 10‰ over depth intervals of 10 m and less. Based on macroscopic textural observations of calcite veins and their stable isotope composition, three different vein generations can be identified, which represent fluid flow during limestone diagenesis and during and after mineralization, respectively. The stable isotope composition of synmineralization veins and their wall rocks is consistent with an advection-dominated reactive flow model and isotope exchange during mineral dissolution-precipitation reactions driven by a large flux of high-temperature magmatic fluid. The correlation of vein calcite trace-element concentrations with stable isotope ratios corroborates their classification as pre-, syn-, and postmineral fluid pathways. The highly variable limestone wall-rock stable isotope composition in the mineralization zone and the existence of wall-rock samples that are isotopically depleted relative to adjacent synmineralization veins imply that fluid flow was locally channelized and aided by brittle deformation. Overall, the lateral extent of detectable stable isotope alteration in proximal and distal holes for up to 10.6 km away from the Upper Manto mineralization along strike of the Finlay Formation defines the size of the stable isotope footprint of the Cinco de Mayo Zn-Ag deposit. Combining this with zoning and variability of stable isotope results indicates that stable isotope studies can aid mineral exploration programs: (1) by defining the magnitude of the overall system, (2) as a vectoring tool, and (3) to identify pathways preferentially followed by the hydrothermal fluids, which may also represent sites for metal accumulation. An example of the practical application of these results is the strong indication that additional exploration potential exists

near proximal hole CM08-45 because its degree of stable isotope alteration is comparable to mineralization zone samples. In addition, the lack of stable isotope ratio transition from altered to background values with depth in CM10-247 suggests that alteration and perhaps mineralization extend to levels deeper than currently captured by exploration drilling.

Acknowledgments

We are grateful to C. Raley and B. Neumann for assistance during laboratory stable isotope analyses. This research has been funded through a MITACS Elevate fellowship to A.B., MAG Silver Corp., and ALS Canada Ltd. Insightful reviews by Lluís Fontboté and Peter Larson greatly helped to improve this contribution.

REFERENCES

Ague, J.J., 1997, Crustal mass transfer and index mineral growth in Barrow's garnet zone, northeast Scotland: Geology, v. 25, p. 73–76.

Albinson, T., Norman, D.I., Cole, D., and Chomiak, B., 2001, Controls on formation of low-sulfidation epithermal deposits in Mexico: Constraints from fluid inclusion and stable isotope data: Society of Economic Geologists, Special Publication no. 8, p. 1–32.

Andrew, B.S., and Barker, S.L.L., 2017, Determination of carbonate vein chemistry using portable X-ray fluorescence and its application to mineral exploration: Geochemistry: Exploration, Environment, Analysis, v. 18, p. 85–93.

Baer, D.S., Paul, J.B., Gupta, M., and O'Keefe, A., 2002, Sensitive absorption measurements in the near-infrared region using off-axis integrated cavity output spectroscopy: SPIE 4817, Diode Lasers and Applications in Atmospheric Sensing, 2002, p. 167–176.

Barker, S.L.L., Dipple, G.M., Dong, F., and Baer, D.S., 2011, Use of laser spectroscopy to measure the $^{13}C/^{12}C$ and $^{18}O/^{16}O$ compositions of carbonate minerals: Analytical Chemistry, v. 83, p. 2220–2226.

Barker, S.L.L., Dipple, G.M., Hickey, K.A., Lepore, W.A., and Vaughan, J.R., 2013, Applying stable isotopes to mineral exploration: teaching an old dog new tricks: Economic Geology, v. 108, p. 1–9.

Bau, M., 1991, Rare-earth element mobility during hydrothermal and metamorphic fluid-rock interaction and the significance of the oxidation state of europium: Chemical Geology, v. 93, p. 219–230.

Bau, M., and Möller, P., 1992, Rare earth element fractionation in metamorphogenic hydrothermal calcite, magnesite and siderite: Mineralogy and Petrology, v. 45, p. 231–246.

Beinlich, A., Barker, S.LL., Dipple, G. M., Gupta, M., and Baer, D. S., 2017, Stable isotope ($\delta^{13}C$, $\delta^{18}O$) analysis of sulfide-bearing carbonate samples using laser absorption spectrometry: Economic Geology, v. 112, p. 693–700.

Bowman, J.R., Willett, S.D., and Cook, S.J., 1994, Oxygen isotopic transport and exchange during fluid-flow: one-dimensional models and applications: American Journal of Science, v. 294, p. 1–55.

Campbell, A.R., and Larson, P.B., 1998, Introduction to stable isotope applications in hydrothermal systems: Reviews in Economic Geology, v. 10, p. 173–194.

Camprubi, A., Gonzalez-Partida, E., and Iriondo, A., 2006, Mineralizing fluids of the shallow epithermal Au-Ag deposits of the El Barqueno district, Jalisco, Mexico: Journal of Geochemical Exploration, v. 89, p. 39–44.

Cathles, L.M., 1993, Oxygen isotope alteration in the Noranda mining district, Abitibi greenstone belt, Quebec: Economic Geology, v. 88, p. 1483–1511.

Chacko, T., Cole, D.R., and Horita, J., 2001, Equilibrium oxygen, hydrogen and carbon isotope fractionation factors applicable to geologic systems: Stable Isotope Geochemistry, v. 43, p. 1–81.

Clark, K.F., and de la Fuente L., F.E., 1978, Distribution of mineralization in time and space in Chihuahua, Mexico: Mineralium Deposita, v. 13, p. 27–49.

Criss, R.E., and Taylor, H.P., 1983, An $^{18}O/^{16}O$ and D/H study of Tertiary hydrothermal systems in the southern half of the Idaho batholith: Geological Society of America Bulletin, v. 94, p. 640–663.

Criss, R.E., Champion, D.E., and Mcintyre, D.H., 1985, Oxygen isotope, aeromagnetic, and gravity-anomalies associated with hydrothermally altered zones in the Yankee Fork mining district, Custer County, Idaho: Economic Geology, v. 80, p. 1277–1296.

Criss, R.E., Singleton, M.J., and Champion, D.E., 2000, Three-dimensional oxygen isotope imaging of convective fluid flow around the Big Bonanza, Comstock lode mining district, Nevada: Economic Geology, v. 95, p. 131–142.

Cumming, G.L., Kesler, S.E., and Krstic, D., 1979, Isotopic composition of lead in Mexican mineral deposits: Economic Geology, v. 74, p. 1395–1407.

Dilles, J.H., Solomon, G.C., Taylor, H.P., and Einaudi, M.T., 1992, Oxygen and hydrogen isotope characteristics of hydrothermal alteration at the Ann-Mason porphyry copper deposit, Yerington, Nevada: Economic Geology, v. 87, p. 44–63.

Dipple, G.M., and Ferry, J.M., 1992a, Fluid flow and stable isotopic alteration in rocks at elevated temperatures with applications to metamorphism: Geochimica et Cosmochimica Acta, v. 56, p. 3539–3550.

——1992b, Metasomatism and fluid-flow in ductile fault zones: Contributions to Mineralogy and Petrology, v. 112, p. 149–164.

Ewers, G.R., Mackenzie, D.E., Wyborn, D., Oversby, B.S., McPhie, J., and Andrews, A., 1994, Regional ^{18}O depletions in igneous rocks from the northern Drummond Basin, Queensland, Australia, and their implications for epithermal gold mineralization: Economic Geology, v. 89, p. 662–673.

Faure, G., and Mensing, T.M., 2005, Isotopes: principles and applications: Hoboken, New Jersey, Wiley, 897 p.

Ferry, J M., and Dipple, G.M., 1991, Fluid-flow, mineral reactions, and metasomatism: Geology, v. 19, p. 211–214.

Ferry, J.M., Wing, B.A., Penniston-Dorland, S.C., and Rumble, D., 2002, The direction of fluid flow during contact metamorphism of siliceous carbonate rocks: new data for the Monzoni and Predazzo aureoles, northern Italy, and a global review: Contributions to Mineralogy and Petrology, v. 142, p. 679–699.

Frimmel, H.E., 1992, Isotopic fronts in hydrothermally mineralized carbonate rocks: Mineralium Deposita, v. 27, p. 257–267.

Gies, H., 1975, Activation possibilities and geochemical correlations of photoluminescing carbonates, particularly calcites: Mineralium Deposita, v. 10, p. 216–227.

Haenggi, W.T., 2002, Tectonic history of the Chihuahua trough, Mexico and adjacent USA, Part II: Mesozoic and Cenozoic: Boletin de la Sociedad Geologica Mexicana, v. 55, p. 38–94.

Handschy, J.W., and Dyer, R., 1987, Polyphase deformation in Sierra del Cuervo, Chihuahua, Mexico: Evidence for ancestral Rocky Mountain tectonics in the Ouachita foreland of northern Mexico: Geological Society of America Bulletin, v. 99, p. 618–632.

Haynes, F.M., and Kesler, S.E., 1988, Compositions and sources of mineralizing fluids for chimney and manto limestone-replacement ores in Mexico: Economic Geology, v. 83, p. 1985–1992.

Hellstrom, J., Paton, C., Woodhead, J., and Hergt, J., 2008, Iolite: software for spatially resolved LA-(quad and MC) ICP-MS analysis: Mineralogical Association of Canada Short Course series, v. 40, p. 343–348.

Hewitt, W.P., 1966, Geology and mineralization of the main mineral zone of the Santa Eulalia district, Chihuahua, Mexico: Boletin de la Sociedad Geologica Mexicana, v. 29, p. 69–147.

Hickey, K.A., Ahmed, A.D., Barker, S.L.L., and Leonardson, R., 2014, Fault-controlled lateral fluid flow underneath and into a Carlin-type gold deposit: Isotopic and geochemical footprints: Economic Geology, v. 109, p. 1431–1460.

Hofmann, A., 1972, Chromatographic theory of infiltration metasomatism and its application to feldspars: American Journal of Science, v. 272, p. 69–90.

Hu, Z.C., Gao, S., Liu, Y.S., Hu, S.H., Chen, H.H., and Yuan, H.L., 2008, Signal enhancement in laser ablation ICP-MS by addition of nitrogen in the central channel gas: Journal of Analytical Atomic Spectrometry, v. 23, p. 1093–1101.

Jamtveit, B., Grorud, H.F., and Bucher-Nurminen, K., 1992, Contact metamorphism of layered carbonate-shale sequences in the Oslo Rift. II: Migration of isotopic and reaction fronts around cooling plutons: Earth and Planetary Science Letters, v. 114, p. 131–148.

Kelley, D.L., Kelley, K.D., Coker, W.B., Caughlin, B., and Doherty, M.E., 2006, Beyond the obvious limits of ore deposits: The use of mineralogical, geochemical, and biological features for the remote detection of mineralization: Economic Geology, v. 101, p. 729–752.

Kesler, S.E., Vennemann, T.W., Vazquez, R., Stegner, D.P., and Frederickson, G.C., 1995, Application of large-scale oxygen isotope haloes to exploration for chimney-manto Pb-Zn-Cu-Ag deposits, *in* Coyner, A.R., and Fahey, P.L., eds., Geology and ore deposits of the American Cordillera: Reno, Geological Society of Nevada, p. 1383–1396.

Klein, T.L., and Criss, R.E., 1988, An oxygen isotope and geochemical study of meteoric-hydrothermal systems at Pilot Mountain and selected other localities, Carolina slate belt: Economic Geology, v. 83, p. 801–821.

Knoop, S.R., Kennedy, L.A., and Dipple, G.M., 2002, New evidence for syntectonic fluid migration across the hinterland-foreland transition of the Canadian Cordillera: Journal of Geophysical Research: Solid Earth, v. 107, p. ETG 6-1-ETG 6-25.

Large, R.R., Bull, S.W., and Winefield, P.R., 2001, Carbon and oxygen isotope halo in carbonates related to the McArthur River (HYC) Zn-Pb-Ag deposit, north Australia: Implications for sedimentation, ore genesis, and mineral exploration: Economic Geology, v. 96, p. 1567–1593.

Larson, P.B., and Taylor, H.P., 1986a, An oxygen-isotope study of water-rock interaction in the granite of Cataract Gulch, western San Juan Mountains, Colorado: Geological Society of America Bulletin, v. 97, p. 505–515.

——1986b, An oxygen isotope study of hydrothermal alteration in the Lake City caldera, San-Juan Mountains, Colorado: Journal of Volcanology and Geothermal Research, v. 30, p. 47–82.

Larson, P.B., Cunningham, C.G., and Naeser, C.W., 1994, Large-scale alteration effects in the Rico paleothermal anomaly, southwest Colorado: Economic Geology, v. 89, p. 1769–1779.

Lassey, K.R., and Blattner, P., 1988, Kinetically controlled oxygen isotope exchange between fluid and rock in one-dimensional advective flow: Geochimica et Cosmochimica Acta, v. 52, p. 2169–2175.

Longerich, H.P., Jackson, S.E., and Gunther, D., 1996, Laser ablation inductively coupled plasma mass spectrometric transient signal data acquisition and analyte concentration calculation: Journal of Analytical Atomic Spectrometry, v. 11, p. 899–904.

Lyons, J.I., 2009, Cinco de Mayo, Chihuahua, Mexico Stratigraphy: Private report for MAG Silver Corp., June 20, 2009, 12 p.

MacInnis, D., 2009, MAG Silver discovers high grade molybdenum with gold at Cinco de Mayo, MAG Silver News Releases, September 23, 2009.

——2010, Cinco de Mayo September 30, 2010 management discussion and analysis ("MD&A") excerpt, with full assay table and illustrative map, MAG Silver News Releases, November 10, 2010.

——2012, MAG Silver drills 61.6 metre silver, gold, zinc, lead, copper massive sulphide intercept at Cinco de Mayo, MAG Silver News Releases, July 18, 2012.

McDowell, F.W., and Keizer, R.P., 1977, Timing of mid-Tertiary volcanism in the Sierra Madre Occidental between Durango City and Mazatlan, Mexico: Geological Society of America Bulletin, v. 88, p. 1479–1487.

McLennan, S.M., 1989, Rare earth elements in sedimentary rocks; influence of provenance and sedimentary processes: Reviews in Mineralogy and Geochemistry, v. 21, p. 169–200.

Megaw, P., MacGlasson, J.A., Lyons, J.I., Hansen, L.D., and MacInnis, D.T., 2014, Blind Ag-Pb-Zn and Au-Mo discoveries in MAG Silver's Cinco de Mayo Mega-System, Chihuahua, Mexico: Society of Economic Geologists, SEG 2014, Keystone, Colorado, Abstracts, no. P176.

Megaw, P.K., M., Barton, M.D., and Falce, J.I., 1996, Carbonate-hosted lead-zinc (Ag, Cu, Au) deposits of northern Chihuahua, Mexico: Society of Economic Geologists, Special Publication no. 4, p. 277–288.

Megaw, P.K.M., 1990, Geology and geochemistry of the Santa Eulalia mining district, Chihuahua, Mexico: Unpublished Ph.D. thesis, Tucson, Arizona, The University of Arizona, 461 p.

Megaw, P.K.M., Ruiz, J., and Titley, S.R., 1988, High-temperature, carbonate-hosted Ag-Pb-Zn(Cu) deposits of northern Mexico: Economic Geology, v. 83, p. 1856–1885.

Meinert, L.D., Dipple, G.M., and Nicolescu, S., 2005, World skarn deposits: Economic Geology 100th Anniversary Volume, p. 299–336.

Millonig, L.J., Beinlich, A., Raudsepp, M., Devine, F., Archibald, D.A., Linnen, R.L., and Groat, L.A., 2017, The Engineer mine, British Columbia: An example of epithermal Au-Ag mineralization with mixed alkaline and subalkaline characteristics: Ore Geology Reviews, v. 83, p. 235–257.

Muehlberger, W.R., 1993, Tectonic map of North America: Southwest and southeast sheets: A user's guide: American Association of Petroleum Geologists, 6 p.

Müller, W., Shelley, M., Miller, P., and Broude, S., 2009, Initial performance metrics of a new custom-designed ArF excimer LA-ICPMS system coupled to a two-volume laser-ablation cell: Journal of Analytical Atomic Spectrometry, v. 24, p. 209–214.

Murakami, H., and Nakano, T., 1999, Hydrothermal alteration of limestone and mineral exploration of Zn-Pb skarn deposits in the Sako-nishi area of the Kamioka mine, Central Japan: Resource Geology, v. 49, p. 259–280.

Naito, K., Fukahori, Y., He, P.M., Sakurai, W., Shimazaki, H., and Matsuhisa, Y., 1995, Oxygen and carbon isotope zonations of wall rocks around the Kamioka Pb-Zn skarn deposits, central Japan: Application to prospecting: Journal of Geochemical Exploration, v. 54, p. 199–211.

Nieto-Samaniego, Á.F., Ferrari, L., Alaniz-Alvarez, S.A., Labarthe-Hernández, G., and Rosas-Elguera, J., 1999, Variation of Cenozoic extension and volcanism across the southern Sierra Madre Occidental volcanic province, Mexico: Geological Society of America Bulletin, v. 111, p. 347–363.

Robertson, K., and Megaw, P., 2009, Cinco de Mayo: A new silver, lead, and zinc discovery in northern Mexico: The Leading Edge, v. 28, p. 730–735.

Ross, D., 2012, Technical report on the Upper Manto deposit, Chihuahua, Mexico: NI 43-101 Report, 98 p.

Ruiz, J., Patchett, P.J., and Ortega-Gutierrez, F., 1988, Proterozoic and Phanerozoic basement terranes of Mexico from Nd isotopic studies: Geological Society of America Bulletin, v. 100, p. 274–281.

Rye, R.O., 1966, The carbon, hydrogen, and oxygen isotopic composition of the hydrothermal fluids responsible for the lead-zinc deposits at Providencia, Zacatecas, Mexico: Economic Geology, v. 61, p. 1399–1427.

Rye, R.O., and O'Neil, J.R., 1968, O^{18} content of water in primary fluid inclusions from Providencia north-central Mexico: Economic Geology, v. 63, p. 232–238.

Schulman, J.H., Evans, L.W., Ginther, R.J., and Murata, K.J., 1947, The sensitized luminescence of manganese-activated calcite: Journal of Applied Physics, v. 18, p. 732–739.

Selway, J., and Leonard, B., 2008, Independent technical report—Cinco de Mayo, Mexico: Sudbury, Ontario, Caracle Creek International Consulting Inc., 152 p.

Shelton, K.L., 1983, Composition and origin of ore-forming fluids in a carbonate-hosted porphyry copper and skarn deposit; a fluid inclusion and stable isotope study of Mines Gaspe, Quebec: Economic Geology, v. 78, p. 387–421.

Sweeney, R.L., 1987, Stable isotope geochemistry of calcite and limestone at Naica, Chihuahua, Mexico: Unpublished M.Sc. thesis, Tucson, Arizona, University of Arizona, 51 p.

Taylor, H.P., 1974, Application of oxygen and hydrogen isotope studies to problems of hydrothermal alteration and ore deposition: Economic Geology, v. 69, p. 843–883.

——1979, Oxygen and hydrogen isotope relationships in hydrothermal mineral deposits, *in* Barnes, H.L., ed., Geochemistry of Hydrothermal Ore Deposits, 2nd ed.: New York, Wiley, p. 236–277.

——1997, Oxygen and hydrogen isotope relationships in hydrothermal mineral deposits, *in* Barnes, H.L., ed., Geochemistry of Hydrothermal Ore Deposits, 3rd ed.: New York, Wiley, p. 229–302.

Taylor, H.P., and Epstein, S., 1963, O^{18}/O^{16} ratios in rocks and coexisting minerals of the Skaergaard Intrusion, east Greenland: Journal of Petrology, v. 4, p. 51–74.

Towell, D.G., Winchester, J.W., and Spirn, R.V., 1965, Rare-earth distributions in some rocks and associated minerals of the batholith of southern California: Journal of Geophysical Research, v. 70, p. 3485–3496.

Vazquez, R., Vennemann, T.W., Kesler, S.E., and Russell, N., 1998, Carbon and oxygen isotope halos in the host limestone, El Mochito Zn-Pb-(Ag) skarn massive sulfide-oxide deposit, Honduras: Economic Geology, v. 93, p. 15–31.

Veizer, J., Ala, D., Azmy, K., Bruckschen, P., Buhl, D., Bruhn, F., Carden, G.A.F., Diener, A., Ebneth, S., Godderis, Y., Jasper, T., Korte, C., Pawellek, F., Podlaha, O.G., and Strauss, H., 1999, $^{87}Sr/^{86}Sr$, delta $\delta^{13}C$ and $\delta^{18}O$ evolution of Phanerozoic seawater: Chemical Geology, v. 161, p. 59–88.

Velador, J.M., Heizler, M.T., and Campbell, A.R., 2010, Timing of magmatic activity and mineralization and evidence of a long-lived hydrothermal system in the Fresnillo silver district, Mexico: Constraints from $^{40}Ar/^{39}Ar$ geochronology: Economic Geology, v. 105, p. 1335–1349.

Waring, C.L., Andrew, A.S., and Ewers, G.R., 1998, Use of O, C, and S stable isotopes in regional mineral exploration: AGSO Journal of Australian Geology & Geophysics, v. 17, p. 301–313.

Andreas Beinlich is currently a Research Fellow at the Institute for Geoscience Research (TIGeR), Curtin University, Australia. Prior to his current position, Andreas was coordinating the Carbonate Alteration Footprints (CAF) project at the Mineral Deposit Research Unit (MDRU), The University of British Columbia, a collaborative research-initiative with MAG Silver, ALS Minerals, Teck, Glencore, and Barrick Gold. Andreas received his Ph.D. from the University of Oslo and did undergraduate research at the Universities of Würzburg, Germany, and Otago, New Zealand. Andreas's field-based and experimental research is focused on hydrothermal rock alteration and fluid flow with environmental and economic relevance.